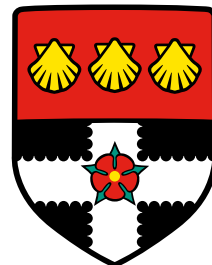


UNIVERSITY OF READING  
DEPARTMENT OF METEOROLOGY



---

## Numerical representation of mountains in atmospheric models

---

James Shaw

TODO: *date*

## Acknowledgements

This research is supported by a PhD studentship funded by NERC grants NE/K500860/1 and NE/L501608/1, and by the University of Reading with CASE support from the UK Met Office. I am indebted to my supervisors, Hilary Weller (University of Reading), John Methven (University of Reading) and Terry Davies (Met Office) for their dedicated support and guidance throughout my time at the University of Reading.

I am very grateful to Hans Johansen (Lawrence Berkeley National Laboratory) for providing the mathematical techniques enabling the development of a high-order transport scheme. The Leibniz Institute for Tropospheric Research kindly provided their cut cell mesh generator, and Christoph Schär (ETH Zürich) provided his transport scheme and test case implementation. I am also grateful to my friend Shing Hing Man for his assistance with cubicFit candidate polynomial generation. I thank the Dynamics Research group at the Met Office, and Tristan Pryer (University of Reading), for many useful discussions. I must also thank my partner Isabel for her patience and encouragement.

This thesis is based upon two journal articles, and I thank the anonymous reviewers for their helpful questions. [Shaw and Weller \(2016\)](#) developed the slanted cell method (section 3.1) and performed those numerical experiments found in sections 2.2, 2.3, 3.4 and 4.1. [Shaw et al. \(2017\)](#) developed the cubicFit transport scheme (chapter 2) and performed those transport tests found in sections 2.4 and 3.2.

Shaw, J., and H. Weller, 2016: Comparison of terrain-following and cut-cell grids using a nonhydrostatic model. *Mon. Wea. Rev.*, **144** (6), 2085–2099, doi:[10.1175/MWR-D-15-0226.1](https://doi.org/10.1175/MWR-D-15-0226.1)

Shaw, J., H. Weller, J. Methven, and T. Davies, 2017: Multidimensional method-of-lines transport for atmospheric flows over steep terrain using arbitrary meshes. *J. Comp. Phys.*, **344**, 86–107, doi:[10.1016/j.jcp.2017.04.061](https://doi.org/10.1016/j.jcp.2017.04.061)

Declaration: I confirm that this is my own work and the use of all material from other sources has been properly and fully acknowledged. — James Shaw

## **Abstract**

Lorem ipsum dolor sit amet, consectetuer adipiscing elit. Etiam lobortis facilisis sem. Nullam nec mi et neque pharetra sollicitudin. Praesent imperdiet mi nec ante. Donec ullamcorper, felis non sodales commodo, lectus velit ultrices augue, a dignissim nibh lectus placerat pede. Vivamus nunc nunc, molestie ut, ultricies vel, semper in, velit. Ut porttitor. Praesent in sapien. Lorem ipsum dolor sit amet, consectetuer adipiscing elit. Duis fringilla tristique neque. Sed interdum libero ut metus. Pellentesque placerat. Nam rutrum augue a leo. Morbi sed elit sit amet ante lobortis sollicitudin. Praesent blandit blandit mauris. Praesent lectus tellus, aliquet aliquam, luctus a, egestas a, turpis. Mauris lacinia lorem sit amet ipsum. Nunc quis urna dictum turpis accumsan semper.

# Contents

---

<b>1</b>	<b>Introduction</b>	<b>1</b>
<b>2</b>	<b>Numerically stable transport over steep slopes</b>	<b>2</b>
2.1	Transport schemes for arbitrary meshes . . . . .	5
2.2	Horizontal transport over mountains . . . . .	17
2.3	Transport in a terrain-following velocity field . . . . .	22
2.4	Deformational flow on a sphere . . . . .	24
<b>3</b>	<b>A new mesh for representing the atmosphere above terrain</b>	<b>29</b>
3.1	Slanted cell method . . . . .	32
3.2	Transport over a mountainous lower boundary . . . . .	33
3.3	Discretisation of the fully compressible Euler equations . . . . .	38
3.4	Stratified atmosphere initially at rest . . . . .	39
<b>4</b>	<b>Generalising the Charney–Phillips staggering for arbitrary meshes</b>	<b>42</b>
4.1	Schär mountain waves . . . . .	42
4.2	Advective-form transport for arbitrary Charney–Phillips meshes . . . . .	45
4.3	A new test case to excite the Lorenz computational mode . . . . .	45
4.4	Horizontal transport on distorted Charney–Phillips meshes . . . . .	45
<b>5</b>	<b>Conclusion</b>	<b>47</b>
	<b>Appendices</b>	<b>48</b>
<b>A</b>	<b>Mesh geometry on a spherical Earth</b>	<b>49</b>
	<b>Bibliography</b>	<b>52</b>

# 1 Introduction

---

## 2 Numerically stable transport over steep slopes

---

---

### Highlights

- The new cubicFit transport scheme is second-order convergent regardless of mesh distortions or the choice of velocity field
  - Sub-grid reconstructions are mostly precomputed depending on the mesh geometry alone
  - Misalignment of the velocity field with mesh layers is the primary source of numerical error, not simply mesh distortions
- 

*TODO: it would be nice to have a citation for each desirable properties demonstrating what can happen if that property is absent*

**Conservation** *Conserve mass for climate runs, conserve moisture to avoid Met Office's 'eternal fountain'*

**Numerical stability** *grid-point storms when CFL is violated – not really the fault of the advection scheme, though!*

**Numerical diffusion** *Schär et al. (2002); Kent et al. (2014) show it happens with horizontal flow on TF meshes. Hoinka and Zängl (2004) show it happens for moisture and momentum advection. How about spurious smoothing of fronts? stable isotopes of water, important for paleoclimate simulations (Cauquoin and Risi, 2017)*

**Numerical dispersion/spurious oscillations** *Spurious oscillations found in many variables: in OLAM (Walko and Avissar, 2008), MC2 (Schär et al., 2002) and MM5 (Hoinka and Zängl, 2004). Also problematic in ocean/sea-ice modelling (Naughten et al., 2017)*

**Better than first-order convergence** *(Staniforth and Thuburn, 2012)*

**Grid imprinting** (*Staniforth and Thuburn, 2012*) *Anyone talk about it in the context of advection? Thuburn et al. (2014) mentions it but his advection scheme shows little sign of grid imprinting*

**Mesh distortions** *Intro already covers this well*

**Time-to-solution** *Intro already covers computational efficiency well*

A huge variety of transport schemes have been developed for atmospheric models, but few are able to account for distortions associated with steep terrain because they treat horizontal and vertical transport separately ([Kent et al., 2014](#)), resulting in numerical errors called ‘splitting errors’. Such errors can be reduced by explicitly accounting for transverse fluxes when combining fluxes ([Leonard et al., 1996](#)), but splitting errors are still apparent in flows over steep terrain where meshes are highly distorted and metric terms in a terrain-following coordinate transform are large ([Chen et al., 2017](#)).

Transport schemes are often classified as dimensionally-split or multidimensional. Dimensionally-split schemes such as ([Lin and Rood, 1996](#); [Guo et al., 2014](#)) calculate transport in each dimension separately before the flux contributions are combined. Such schemes are computationally efficient and allow existing one-dimensional high-order methods to be used. When dimensionally-split schemes are used for horizontal transport, quadrilateral meshes are needed because the mesh dimensions are inherently separable. Special treatment is required at the corners of cubed-sphere panels where local coordinates differ ([Putman and Lin, 2007](#); [Guo et al., 2014](#)). Dimensional splitting is often used for vertical transport and, for similar reasons, dimensionally-split schemes have only been used with terrain-following coordinate transforms and not cut cells. Perhaps confusingly, dimensionally-split schemes are sometimes called multidimensional, too, because they use one-dimensional techniques for multidimensional transport.

Unlike dimensionally-split schemes, multidimensional schemes consider transport in two or three dimensions together. There are several subclasses of multidimensional schemes that include semi-Lagrangian finite volume schemes (also called conservative mesh remapping), swept-area schemes (also called flux-form semi-Lagrangian, incremental remapping, or forward-in-time), and method-of-lines schemes (also called Eulerian schemes). Two-dimensional semi-Lagrangian finite volume schemes such as ([Iske and Käser, 2004](#); [Lauritzen et al., 2010](#)) integrate over departure cells that are found by tracing backward the trajectories of cell vertices. These schemes are conservative because departure cells are constructed so that there are no overlaps or gaps, which requires that cell areas are simply-connected domains ([Lauritzen et al., 2011b](#)). SLICE-3D is a three-dimensional semi-Lagrangian finite volume scheme for latitude-longitude meshes that applies separate conservative remappings in each dimension ([Zerroukat and Allen, 2012](#)). Swept area schemes such as ([Lashley, 2002](#); [Skamarock and Menchaca, 2010](#); [Lauritzen et al., 2011a](#); [Thuburn et al., 2014](#)) calculate the flux through a cell face by integrating over the upstream area that is swept out over one time-step. Such schemes differ in their choice of area approximation, sub-grid reconstruction, and spatial integration method. Because swept area schemes integrate over the reconstructed field, they typically require a matrix-vector multiply per face per time-stage ([Thuburn et al., 2014](#); [Skamarock and Menchaca, 2010](#)). Method-of-lines schemes such

as (Weller et al., 2009; Skamarock and Gassmann, 2011) use a spatial discretisation to reduce the transport PDE to an ODE that is typically solved using a multi-stage time-stepping method. A method-of-lines scheme using a spectral element reconstruction was recently developed to achieve accurate solutions near the surface of cut cell meshes (Steppeler and Klemp, 2017). Unlike semi-Lagrangian finite volume schemes, swept-area and method-of-lines schemes achieve conservation for small-scale rotational flows. Such flows can twist the departure domain to such an extent that the domain intersects itself (Lauritzen et al., 2011a). In two dimensions, a self-intersecting departure domain has a bowtie or hourglass shape. There are many more types of atmospheric transport schemes, but all can be classified according to their treatment of the three spatial dimensions. A more comprehensive overview is presented by Lauritzen et al. (2014).

For transport schemes that are ordinarily classified as ‘multidimensional’, a further distinction ought to made between horizontally-multidimensional and three-dimensional schemes. Most multidimensional schemes are only horizontally-multidimensional because, while the two horizontal dimensions are considered together, horizontal and vertical transport are still treated separately. This separate treatment becomes less justifiable as atmospheric models are using increasingly fine horizontal mesh spacings that resolve small-scale steep slopes, resulting in greater mesh distortion and possible splitting errors (Kent et al., 2014). Three-dimensional schemes avoid any splitting errors over steep slopes, but only a few conservative three-dimensional schemes have been used in atmospheric models. The multi-moment constrained finite volume scheme (Li and Xiao, 2009) is a three-dimensional scheme that has been used to simulate non-hydrostatic flows over orography with terrain-following coordinates on a  $x-z$  plane (Li et al., 2013). Simulations of subcritical flow around a cylinder have also been performed on a three-dimensional hexahedral-prismatic hybrid mesh (Xie and Xiao, 2016). The Multidimensional Positive Definite Advection Transport Algorithm (MPDATA) is another three-dimensional scheme that is suitable for arbitrary meshes. It has been used on triangular unstructured meshes to simulate two-dimensional nonhydrostatic flows over orography (Smolarkiewicz and Szmelter, 2011), and in three-dimensional transport tests (Smolarkiewicz and Szmelter, 2005). Most recently, Kühnlein and Smolarkiewicz (2017) extended MPDATA to enable semi-implicit integrations of the compressible Euler equations on arbitrary meshes. The three-dimensional method-of-lines scheme developed by Weller and Shahrokhi (2014) has been used in two-dimensional flows over orography on Cartesian  $x-z$  planes with distorted meshes (Chen et al., 2017). This finite volume scheme uses a moving least-squares reconstruction that makes it suitable for arbitrary meshes. This least-squares approach has been applied previously to shallow water flows (Cueto-Felgueroso et al., 2006), aeronautic (Cueto-Felgueroso et al., 2007) and porous media (White et al., 2017) simulations.

This chapter presents a new multidimensional method-of-lines scheme, ‘cubicFit’, that improves the stability of the scheme by Weller and Shahrokhi (2014) and avoids all splitting errors. To reconstruct values at cell faces, the scheme fits a multidimensional cubic polynomial over an upwind-biased stencil using a least-squares approach. The implementation uses stability con-

ditions derived from a von Neumann stability analysis to select appropriate polynomial fits for stencils in highly-distorted mesh regions. Almost all of the least-squares procedure depends upon the mesh geometry only and reconstruction weights can be precomputed without knowledge of the velocity field or tracer field. Hence, the computational cost of the cubicFit scheme is lower than most swept-area schemes that require a matrix-vector multiply per face per time-stage. Instead, the computational cost is more comparable to dimensionally-split schemes, with the cubicFit scheme requiring only  $n$  multiplies per face per time-stage where  $n$  is the size of the stencil.

The remainder of this chapter is organised as follows. Section 2.1 starts by discretising the transport equation using a method-of-lines approach before describing the cubicFit transport scheme and a multidimensional linear upwind transport scheme. Subsequent sections evaluate the cubicFit scheme in a series of three idealised numerical tests. The test in section 2.2 follows Schär et al. (2002), transporting a tracer horizontally above steep mountains on two-dimensional, highly-distorted terrain-following meshes. Section 2.3 formulates a new tracer transport test that uses a terrain-following velocity field to challenge transport schemes on cut cell meshes. Finally, in section 2.4, we assess the cubicFit transport scheme on hexagonal-icosahedral meshes and cubed-sphere meshes using a standard test of deformational flow on a single-layer spherical Earth, as specified by Lauritzen et al. (2012).

## 2.1 Transport schemes for arbitrary meshes

The transport of a dependent variable  $\phi$  in a prescribed, non-divergent velocity field  $\mathbf{u}$  is given by the equation

$$\frac{\partial \phi}{\partial t} + \nabla \cdot (\mathbf{u}\phi) = 0. \quad (2.1)$$

The time derivative is discretised using a two-stage, second-order Heun method,

$$\phi^* = \phi^{(n)} + \Delta t g(\phi^{(n)}) \quad (2.2a)$$

$$\phi^{(n+1)} = \phi^{(n)} + \frac{\Delta t}{2} [g(\phi^{(n)}) + g(\phi^*)] \quad (2.2b)$$

where  $g(\phi^{(n)}) = -\nabla \cdot (\mathbf{u}\phi^{(n)})$  at time level  $n$ . The same time-stepping method is used for both the cubicFit scheme and the multidimensional linear upwind scheme. Although the Heun method is unstable for a linear oscillator (Durran, 2013) and for solving the transport equation using centred, linear differencing, it is stable when it is used for transport schemes with sufficient upwinding.

Using the finite volume method, the velocity field is prescribed at face centroids and the dependent variable is stored at cell centroids. The divergence term in equation (2.1) is discretised using Gauss's theorem:

$$\nabla \cdot (\mathbf{u}\phi) \approx \frac{1}{\gamma_c} \sum_{f \in c} \mathbf{u}_f \cdot \mathbf{s}_f \phi_f \quad (2.3)$$

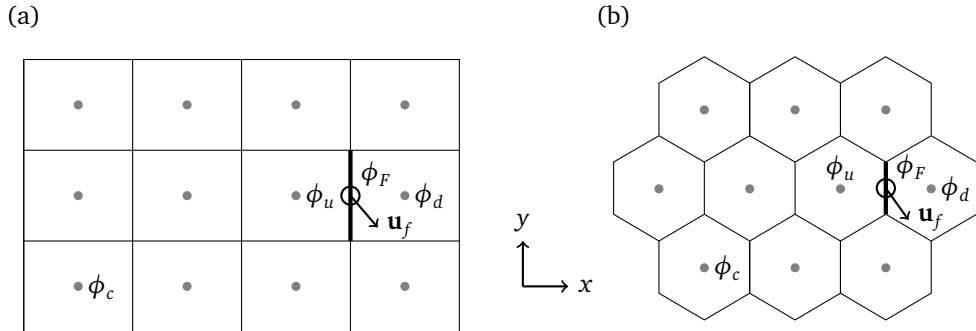


Figure 2.1: Upwind-biased stencils for faces far away from the boundaries of two-dimensional (a) rectangular and (b) hexagonal meshes. The stencil is used to fit a multidimensional polynomial to cell centre values,  $\phi_c$ , marked by grey circles, in order to approximate the value  $\phi_F$  at the face centroid marked by an open circle.  $\phi_u$  and  $\phi_d$  are the values at the centroids of the upwind and downwind cells neighbouring the target face, drawn with a heavy line. The velocity vector  $\mathbf{u}_f$  is prescribed at face  $f$  and determines the choice of stencil at each time-step.

where subscript  $f$  denotes a value stored at a face and subscript  $F$  denotes a value approximated at a face from surrounding values.  $\mathcal{V}_c$  is the cell volume,  $\mathbf{u}_f$  is a velocity vector prescribed at a face,  $\mathbf{S}_f$  is the surface area vector with a direction outward normal to the face and a magnitude equal to the face area,  $\phi_F$  is an approximation of the dependent variable at the face, and  $\sum_{f \in c}$  denotes a summation over all faces  $f$  bordering cell  $c$ . Note that equation (2.3) is a second-order approximation of the divergence term which limits the cubicFit transport scheme to second-order numerical convergence.

This discretisation is applicable to arbitrary meshes. A necessary condition for stability is given by the multidimensional Courant number,

$$\text{Co}_c = \frac{\Delta t}{2\mathcal{V}_c} \sum_{f \in c} |\mathbf{u} \cdot \mathbf{S}_f| \quad (2.4)$$

such that, for all cells  $c$  in the domain,  $\text{Co}_c$  is less than or equal to some constant that depends upon the spatial and temporal discretisation. Hence, stability is constrained by the maximum Courant number of any cell in the domain.

The accurate approximation of the dependent variable at the face,  $\phi_F$ , is key to the overall accuracy of the transport scheme. The cubicFit scheme and multidimensional linear upwind scheme differ in their approximations, and these approximation methods are described next.

### Cubic fit transport scheme

The cubicFit scheme approximates the value of the dependent variable at the face,  $\phi_F$ , using a least-squares fit over a stencil of surrounding known values. To introduce the approximation method, we will consider how an approximate value is calculated for a face that is far away from the boundaries of a two-dimensional uniform rectangular mesh. For any mesh, every interior face connects two adjacent cells. The velocity direction at the face determines which of the two

adjacent cells is the upwind cell. Since the stencil is upwind-biased and asymmetric, two stencils must be constructed for every interior face, and the appropriate stencil is chosen depending on the velocity direction at each face for every time-step.

The upwind-biased stencil for a face  $f$  is shown in figure 2.1a. The wind at the face,  $\mathbf{u}_f$ , is blowing from the upwind cell  $c_u$  to the downwind cell  $c_d$ . To obtain an approximate value at  $f$ , a polynomial least-squares fit is calculated using the stencil values. The stencil has 4 points in  $x$  and 3 points in  $y$ , leading to a natural choice of polynomial that is cubic in  $x$  and quadratic in  $y$ ,

$$\phi = a_1 + a_2x + a_3y + a_4x^2 + a_5xy + a_6y^2 + a_7x^3 + a_8x^2y + a_9xy^2. \quad (2.5)$$

A least-squares approach is needed because the system of equations is overconstrained, with 12 stencil values but only 9 polynomial terms. The stencil geometry is expressed in a local coordinate system with the face centroid as the origin so that the approximated value  $\phi_f$  is equal to the constant coefficient  $a_1$ . The stencil is upwind-biased to improve numerical stability, and the multidimensional cubic polynomial is chosen to improve accuracy in the direction of flow (Leonard et al., 1993).

The remainder of this section generalises the approximation technique for arbitrary meshes and describes the methods for constructing stencils, performing a least-squares fit with a suitable polynomial, and ensuring numerical stability of the transport scheme.

### Stencil construction

For every interior face, two stencils are constructed, one for each of the possible upwind cells. Stencils are not constructed for boundary faces because values of  $\phi$  at boundaries are calculated from prescribed boundary conditions. For a given interior face  $f$  and upwind cell  $c_u$ , we find those faces that are connected to  $c_u$  and ‘oppose’ face  $f$ . These are called the *opposing faces*. The opposing faces for face  $f$  and upwind cell  $c_u$  are determined as follows. Defining  $G$  to be the set of faces other than  $f$  that border cell  $c_u$ , we calculate the ‘opposedness’,  $\text{Opp}$ , between faces  $f$  and  $g \in G$ , defined as

$$\text{Opp}(f, g) \equiv -\frac{\mathbf{S}_f \cdot \mathbf{S}_g}{|\mathbf{S}_f|^2} \quad (2.6)$$

where  $\mathbf{S}_f$  and  $\mathbf{S}_g$  are the surface area vectors pointing outward from cell  $c_u$  for faces  $f$  and  $g$  respectively. Using the fact that  $\mathbf{a} \cdot \mathbf{b} = |\mathbf{a}| |\mathbf{b}| \cos(\theta)$  we can rewrite equation (2.6) as

$$\text{Opp}(f, g) = -\frac{|\mathbf{S}_g|}{|\mathbf{S}_f|} \cos(\theta) \quad (2.7)$$

where  $\theta$  is the angle between faces  $f$  and  $g$ . In this form, it can be seen that  $\text{Opp}$  is a measure of the relative area of  $g$  and how closely it parallels face  $f$ .

The set of opposing faces,  $\text{OF}$ , is a subset of  $G$ , comprising those faces with  $\text{Opp} \geq 0.5$ , and the face with the maximum opposedness. Expressed in set notation, this is

$$\text{OF}(f, c_u) \equiv \{g : \text{Opp}(f, g) \geq 0.5\} \cup \{g : \max_{g \in G}(\text{Opp}(f, g))\}. \quad (2.8)$$

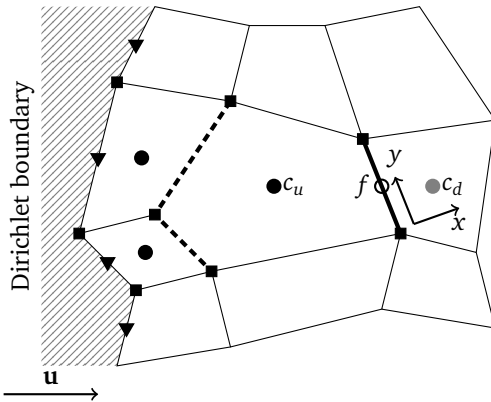


Figure 2.2: A fourteen-point, upwind-biased stencil for face  $f$  connecting the pentagonal upwind cell,  $c_u$ , and the downwind cell  $c_d$ . The dashed lines denote the two faces of cell  $c_u$  that oppose  $f$ , and black circles mark the centroids of the internal cells that are connected to these two opposing faces. The stencil is extended outwards by including cells that share vertices with the three internal cells, where black squares mark these vertices. Four stencil boundary faces, marked by black triangles, are also included. The local coordinate system  $(x, y)$  has its origin at the centroid of face  $f$ , marked by an open circle, with  $x$  normal to  $f$  and  $y$  perpendicular to  $x$ .

On a rectangular mesh, there is always one opposing face  $g$ , and it is exactly parallel to the face  $f$  such that  $\text{Opp}(f, g) = 1$ .

Once the opposing faces have been determined, the set of internal and external cells must be found. The *internal cells* are those cells that are connected to the opposing faces. Note that  $c_u$  is always an internal cell. The *external cells* are those cells that share vertices with the internal cells. Note that  $c_d$  is always an external cell. Finally, the *stencil boundary faces* are boundary faces having Dirichlet boundary conditions<sup>1</sup> that share a vertex with the internal cells. Having found these three sets, the stencil is constructed to comprise all internal cells, external cells and stencil boundary faces.

Figure 2.2 illustrates a stencil construction for face  $f$  connecting upwind cell  $c_u$  and downwind cell  $c_d$ . The two opposing faces are denoted by thick dashed lines and the centres of the three adjoining internal cells are marked by black circles. The stencil is extended outwards by including the external cells that share vertices with the internal cells, where the vertices are marked by black squares. A boundary at the far left has Dirichlet boundary conditions, and so the four stencil boundary faces are also included in the stencil, where the boundary face centres are marked by black triangles. The resultant stencil contains fourteen points.

---

<sup>1</sup>Boundary faces with Neumann boundary conditions would require extrapolated boundary values to be calculated. This would create a feedback loop in which boundary values are extrapolated from interior values, then interior values are transported using stencils that include boundary values. We have not considered how such an extrapolation could be made consistent with the multidimensional polynomial reconstruction. Hence, boundary faces with Neumann boundary conditions are excluded from the set of stencil boundary faces.

### Least-squares fit

To approximate the value of  $\phi$  at a face  $f$ , a least-squares fit is calculated from a stencil of surrounding known values. First, we will show how a polynomial least-squares fit is calculated for a face on a rectangular mesh. Second, we will make modifications to the least-squares fit that are necessary for numerical stability.

For faces that are far away from the boundaries of a rectangular mesh, we fit the multidimensional polynomial given by equation (2.5) that has nine unknown coefficients,  $\mathbf{a} = a_1 \dots a_9$ , using the twelve cell centre values from the upwind-biased stencil,  $\boldsymbol{\phi} = \phi_1 \dots \phi_{12}$ . This yields a matrix equation

$$\begin{bmatrix} 1 & x_1 & y_1 & x_1^2 & x_1y_1 & y_1^2 & x_1^3 & x_1^2y_1 & x_1y_1^2 \\ 1 & x_2 & y_2 & x_2^2 & x_2y_2 & y_2^2 & x_2^3 & x_2^2y_2 & x_2y_2^2 \\ \vdots & \vdots \\ 1 & x_{12} & y_{12} & x_{12}^2 & x_{12}y_{12} & y_{12}^2 & x_{12}^3 & x_{12}^2y_{12} & x_{12}y_{12}^2 \end{bmatrix} \begin{bmatrix} a_1 \\ a_2 \\ \vdots \\ a_9 \end{bmatrix} = \begin{bmatrix} \phi_1 \\ \phi_2 \\ \vdots \\ \phi_{12} \end{bmatrix} \quad (2.9)$$

which can be written as

$$\mathbf{B}\mathbf{a} = \boldsymbol{\phi}. \quad (2.10)$$

The rectangular matrix  $\mathbf{B}$  has one row for each cell in the stencil and one column for each term in the polynomial.  $\mathbf{B}$  is called the *stencil matrix*, and it is constructed using only the mesh geometry. A local coordinate system is established in which  $x$  is normal to the face  $f$  and  $y$  is perpendicular to  $x$ . The coordinates  $(x_i, y_i)$  give the position of the centroid of the  $i$ th cell in the stencil. A two-dimensional stencil is also used for the tests on spherical meshes in section 2.4. In these tests, cell centres are projected perpendicular to a tangent plane at the face centre. Previous studies found that results were largely insensitive to the projection method ([Skamarock and Gassmann, 2011](#); [Lashley, 2002](#)).

The unknown coefficients  $\mathbf{a}$  are calculated using the pseudo-inverse,  $\mathbf{B}^+$ , found by singular value decomposition,

$$\mathbf{a} = \mathbf{B}^+ \boldsymbol{\phi}. \quad (2.11)$$

Recall that the approximate value  $\phi_F$  is equal to the constant coefficient  $a_1$ , which is a weighted mean of  $\boldsymbol{\phi}$ ,

$$a_1 = \begin{bmatrix} b_{1,1}^+ \\ b_{1,2}^+ \\ \vdots \\ b_{1,12}^+ \end{bmatrix} \cdot \begin{bmatrix} \phi_1 \\ \phi_2 \\ \vdots \\ \phi_{12} \end{bmatrix} \quad (2.12)$$

where the weights  $b_{1,1}^+ \dots b_{1,12}^+$  are the elements of the first row of  $\mathbf{B}^+$ . Note that the majority of the least-squares fit procedure depends on the mesh geometry only. An implementation may precompute the pseudo-inverse for each stencil during model initialisation, and only the first

row needs to be stored. Since each face has two possible stencils depending on the orientation of the velocity relative to the face, the implementation stores two sets of weights for each face. Knowledge of the values of  $\phi$  is only required to calculate the weighted mean given by equation (2.12), which is evaluated once per face per time-stage.

In the least-squares fit presented above, all stencil values contributed equally to the polynomial fit. It is necessary for numerical stability that the polynomial fits the cells connected to face  $f$  more closely than other cells in the stencil, as shown by Lashley (2002); Skamarock and Menchaca (2010). To achieve this, we allow each cell to make an unequal contribution to the least-squares fit. We assign an integer *multiplier* to each cell in the stencil,  $\mathbf{m} = m_1 \dots m_{12}$ , and multiply equation (2.10) to obtain

$$\tilde{\mathbf{B}}\mathbf{a} = \mathbf{m} \cdot \phi \quad (2.13)$$

where  $\tilde{\mathbf{B}} = \mathbf{MB}$  and  $\mathbf{M} = \text{diag}(\mathbf{m})$ . The constant coefficient  $a_1$  is calculated from the pseudo-inverse,  $\tilde{\mathbf{B}}^+$ ,

$$a_1 = \tilde{\mathbf{b}}_1^+ \cdot \mathbf{m} \cdot \phi \quad (2.14)$$

where  $\tilde{\mathbf{b}}_1^+ = \tilde{b}_{1,1}^+ \dots \tilde{b}_{1,12}^+$  are the elements of the first row of  $\tilde{\mathbf{B}}^+$ . Again,  $a_1$  is a weighted mean of  $\phi$ , where the weights are now  $\tilde{\mathbf{b}}_1^+ \cdot \mathbf{m}$ . Values for  $\mathbf{m}$  are chosen so that the cells connected to face  $f$  make a greater contribution to the least-squares fit, as discussed later in section 2.1.

For faces of a non-rectangular mesh, or faces that are near a boundary, the number of stencil points and number of polynomial terms may differ: a stencil will have one or more cells and, for two-dimensional meshes, its polynomial will have between one and nine terms. Additionally, the polynomial cannot have more terms than its stencil has cells because this would lead to an underconstrained system of equations. The procedure for choosing suitable polynomials is discussed next.

### Polynomial generation

The majority of faces on a uniform two-dimensional mesh have stencils with more than nine cells. For example, a rectangular mesh has 12 points (figure 2.1a), and a hexagonal mesh has 10 points (figure 2.1b). In both cases, constructing a system of equations using the nine-term polynomial in equation (2.5) leads to an overconstrained problem that can be solved using least-squares. However, this is not true for faces near boundaries: stencils that have fewer than nine cells (figure 2.3a) would result in an underconstrained problem, and stencils that have exactly nine cells may lack sufficient information to constrain high-order terms. For example, the stencil in figure 2.3b lacks sufficient information to fit the  $x^3$  term. In such cases, it becomes necessary to perform a least-squares fit using a polynomial with fewer terms.

For every stencil, we find a set of *candidate polynomials* that do not result in an underconstrained problem. In two dimensions, a candidate polynomial has some combination of between one and nine terms from equation (2.5). There are two additional constraints that a candidate polynomial must satisfy.

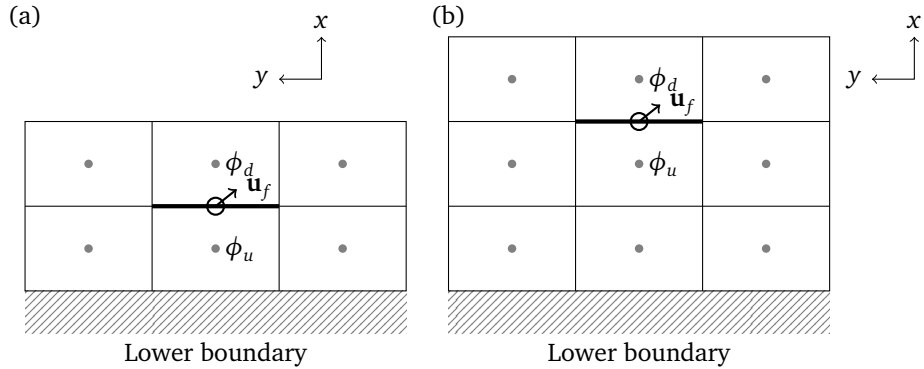


Figure 2.3: Upwind-biased stencils for faces near the lower boundary of a rectangular  $x$ - $z$  mesh, with (a) a  $3 \times 2$  stencil for the face immediately adjacent to the lower boundary, and (b) a  $3 \times 3$  stencil for the face immediately adjacent to the face in (a). Each stencil belongs to the face marked by a thick line. The local coordinate system is shown, having an  $x$  direction normal to the face a  $y$  direction tangent to the face. For both stencils, attempting a least-squares fit using the nine-term polynomial in equation (2.5) would result in an underconstrained problem. There is no normal flow at the lower boundary.

First, high-order terms may be included in a candidate polynomial only if the lower-order terms are also included. More precisely, let

$$M(x, y) = x^i y^j : i, j \geq 0 \text{ and } i \leq 3 \text{ and } j \leq 2 \text{ and } i + j \leq 3 \quad (2.15)$$

be the set of all monomials of degree at most 3 in  $x, y$ . A subset  $S$  of  $M(x, y)$  is “dense” if, whenever  $x^a y^b$  is in  $S$ , then  $x^i y^j$  is also in  $S$  for all  $0 \leq i \leq a$ ,  $0 \leq j \leq b$ . For example, the polynomial  $\phi = a_1 + a_2 x + a_3 y + a_4 xy + a_5 x^2 + a_6 x^2 y$  is a dense subset of  $M(x, y)$ , but  $\phi = a_1 + a_2 x + a_3 y + a_4 x^2 y$  is not because  $x^2 y$  can be included only if  $xy$  and  $x^2$  are also included. In total there are 26 dense subsets of the two-dimensional polynomial in equation (2.5).

Second, a candidate polynomial must have a stencil matrix  $\mathbf{B}$  that is full rank. The matrix is considered full rank if its smallest singular value is greater than  $1 \times 10^{-9}$ . Using a polynomial with all nine terms and the stencil in figure 2.3b results in a rank-deficient matrix and so the nine-term polynomial is not a candidate polynomial.

The candidate polynomials are all the dense subsets of  $M(x, y)$  that have a cardinality greater than one with a stencil matrix that is full rank. The final stage of the cubicFit transport scheme selects a candidate polynomial and ensures that the least-squares fit is numerically stable.

### Achieving numerical stability

So far, we have constructed a stencil and found a set of candidate polynomials. Applying a least-squares fit to any of these candidate polynomials avoids creating an underconstrained problem. The final stage of the transport scheme chooses a suitable candidate polynomial and appropriate multipliers  $\mathbf{m}$  so that the fit is numerically stable.

The approximated value  $\phi_F$  is equal to  $a_1$  which is calculated from equation (2.14). The value of  $a_1$  is a weighted mean of  $\phi$  where  $\mathbf{w} = \tilde{\mathbf{b}}_1^+ \cdot \mathbf{m}$  are the weights. If the cell centre values  $\phi$  are assumed to approximate a smooth field then we expect  $\phi_F$  to be close to the values of  $\phi_u$  and  $\phi_d$ , and expect  $\phi_F$  to be insensitive to small changes in  $\phi$ . When the weights  $\mathbf{w}$  have large magnitude then this is no longer true:  $\phi_F$  becomes sensitive to small changes in  $\phi$  which can result in large, numerically unstable departures from the smooth field  $\phi$ .

To avoid numerical instabilities, simplified, one-dimensional von Neumann analyses were performed in order to impose stability conditions on the weights  $\mathbf{w}$ . The first analysis uses a two-cell approximation to derive separate stability conditions involving the upwind weight  $w_u$  and downwind weight  $w_d$ . The second analysis uses three cells to derive a stability condition that involves all weights in a stencil.

The two-cell analysis starts with the conservation equation for a dependent variable  $\phi$  that is discrete-in-space and continuous-in-time

$$\frac{\partial \phi_j}{\partial t} = -v \frac{\phi_R - \phi_L}{\Delta x} \quad (2.16)$$

where  $v$  is the velocity, and the left and right fluxes,  $\phi_L$  and  $\phi_R$ , are weighted averages of the neighbouring cell centres. Assuming that  $v$  is positive

$$\phi_L = \alpha_u \phi_{j-1} + \alpha_d \phi_j \quad (2.17)$$

$$\phi_R = \beta_u \phi_j + \beta_d \phi_{j+1} \quad (2.18)$$

where  $\phi_{j-1}, \phi_j, \phi_{j+1}$  are cell centre values, and  $j$  denotes a cell centre position  $x = j\Delta x$  where  $\Delta x$  is a uniform mesh spacing.  $\alpha_u$  and  $\beta_u$  are the upwind weights and  $\alpha_d$  and  $\beta_d$  are the downwind weights for the left and right fluxes respectively, and  $\alpha_u + \alpha_d = 1$  and  $\beta_u + \beta_d = 1$ .

At a given time  $t = n\Delta t$  at time-level  $n$  and with a time-step  $\Delta t$ , we assume a wave-like solution with an amplification factor  $A$ , such that

$$\phi_j^{(n)} = A^n e^{ijk\Delta x} \quad (2.19)$$

where  $\phi_j^{(n)}$  denotes a value of  $\phi$  at position  $j$  and time-level  $n$ . Using this to rewrite the left-hand side of equation (2.16)

$$\frac{\partial \phi_j}{\partial t} = \frac{\partial}{\partial t} (A^{t/\Delta t}) e^{ijk\Delta x} = \frac{\ln A}{\Delta t} A^n e^{ijk\Delta x} \quad (2.20)$$

hence equation (2.16) becomes

$$\frac{\ln A}{\Delta t} = -\frac{v}{\Delta x} (\beta_u + \beta_d e^{ik\Delta x} - \alpha_u e^{-ik\Delta x} - \alpha_d) \quad (2.21)$$

$$\ln A = -c (\beta_u - \alpha_d + \beta_d \cos k\Delta x + i\beta_d \sin k\Delta x - \alpha_u \cos k\Delta x + i\alpha_u \sin k\Delta x) \quad (2.22)$$

where the Courant number  $c = v\Delta t/\Delta x$ . Let  $\Re = \beta_u - \alpha_d + \beta_d \cos k\Delta x - \alpha_u \cos k\Delta x$  and  $\Im = \beta_d \sin k\Delta x + \alpha_u \sin k\Delta x$ , then

$$\ln A = -c (\Re + i\Im) \quad (2.23)$$

$$A = e^{-c\Re} e^{-ic\Im} \quad (2.24)$$

and the complex modulus of  $A$  is

$$|A| = e^{-c\Re} = \exp(-c(\beta_u - \alpha_d + (\beta_d - \alpha_u) \cos k\Delta x)) . \quad (2.25)$$

For stability we need  $|A| \leq 1$  and, imposing the additional constraints that  $\alpha_u = \beta_u$  and  $\alpha_d = \beta_d$ , then

$$(\alpha_u - \alpha_d)(1 - \cos k\Delta x) \geq 0 \quad \forall k\Delta x \quad (2.26)$$

and, given  $0 \leq 1 - \cos k\Delta x \leq 2$ , then

$$\alpha_u - \alpha_d \geq 0 . \quad (2.27)$$

Additionally, we do not want more damping than a first-order upwind scheme (where  $\alpha_u = \beta_u = 1$ ,  $\alpha_d = \beta_d = 0$ ), having an amplification factor,  $A_{\text{up}}$ , so we need  $|A| \geq |A_{\text{up}}|$ , hence

$$\exp(-c(\alpha_u - \alpha_d)(1 - \cos k\Delta x)) \geq \exp(-c(1 - \cos k\Delta x)) \quad \forall k\Delta x \quad (2.28)$$

therefore

$$\alpha_u - \alpha_d \leq 1 . \quad (2.29)$$

Now, knowing that  $\alpha_u + \alpha_d = 1$  (or  $\alpha_d = 1 - \alpha_u$ ) then, using equations (2.27) and (2.29), we obtain the first two stability conditions,

$$0.5 \leq \alpha_u \leq 1 \text{ and} \quad (2.30)$$

$$0 \leq \alpha_d \leq 0.5 . \quad (2.31)$$

The three-cell analysis starts again from equation (2.16) but this time approximate  $\phi_L$  and  $\phi_R$  using three cell centre values,

$$\phi_L = \alpha_{uu}\phi_{j-2} + \alpha_u\phi_{j-1} + \alpha_d\phi_j \quad (2.32)$$

$$\phi_R = \alpha_{uu}\phi_{j-1} + \alpha_u\phi_j + \alpha_d\phi_{j+1} \quad (2.33)$$

having used the same weights  $\alpha_{uu}$ ,  $\alpha_u$  and  $\alpha_d$  for both left and right fluxes. Substituting equation (2.19) into equation (2.16) we find

$$A = \exp\left(-c\left[\alpha_{uu}(e^{-ik\Delta x} - e^{-2ik\Delta x}) + \alpha_u(1 - e^{-ik\Delta x}) + \alpha_d(e^{ik\Delta x} - 1)\right]\right) \quad (2.34)$$

so that, if the complex modulus  $|A| \leq 1$  then

$$\alpha_u - \alpha_d + (\alpha_{uu} - \alpha_u + \alpha_d) \cos k\Delta x - \alpha_{uu} \cos 2k\Delta x \geq 0 . \quad (2.35)$$

If  $k\Delta x = \pi$  then  $\cos k\Delta x = -1$  and  $\cos 2k\Delta x = 1$  and  $\alpha_u - \alpha_d \geq \alpha_{uu}$ . If  $k\Delta x = \pi/2$  then  $\cos k\Delta x = 0$  and  $\cos 2k\Delta x = -1$  and  $\alpha_u - \alpha_d \geq -\alpha_{uu}$ . Hence we find that

$$\alpha_u - \alpha_d \geq |\alpha_{uu}| . \quad (2.36)$$

When the same analysis is performed with four cells,  $\alpha_{uuu}$ ,  $\alpha_{uu}$ ,  $\alpha_u$  and  $\alpha_d$ , by varying  $k\Delta x$  we find that equation (2.36) holds replacing  $|\alpha_{uu}|$  with  $\max(|\alpha_{uu}|, |\alpha_{uuu}|)$ . Hence, we generalise equation (2.36) to obtain the final stability condition

$$\alpha_u - \alpha_d \geq \max_{p \in P} |\alpha_p| \quad (2.37)$$

where the peripheral cells  $P$  is the set of all stencil cells except for the upwind cell and downwind cell, and  $\alpha_p$  is the weight for a given peripheral cell  $p$ . The three stability conditions (equations 2.30, 2.31 and 2.36) are used to impose three stability conditions on the weights  $\mathbf{w}$ ,

$$0.5 \leq w_u \leq 1 \quad (2.38a)$$

$$0 \leq w_d \leq 0.5 \quad (2.38b)$$

$$w_u - w_d \geq \max_{p \in P} (|w_p|) \quad (2.38c)$$

where  $w_u$  and  $w_d$  are the weights for the upwind and downwind cells respectively. The *peripheral points*  $P$  are the cells in the stencil that are not the upwind or downwind cells, and  $w_p$  is the weight for a given peripheral point  $p$ . The upwind, downwind and peripheral weights sum to one such that  $w_u + w_d + \sum_{p \in P} w_p = 1$ . We hypothesise that the stability conditions given by equation (2.38) are necessary but not sufficient for a transport scheme on arbitrary meshes.

The stability of the one-dimensional transport equation discretised in space and time could be analysed using existing techniques (Baldauf, 2008), but we have only analysed the spatial stability of the cubicFit scheme. Numerical experiments presented in section 3.2 demonstrate that the cubicFit scheme is generally insensitive to the time-step, provided that it is below a stability limit.

### Stabilisation procedure

Equipped with three stability conditions in equation 2.38, we develop a stabilisation procedure that achieves numerical stability on arbitrary meshes. The stabilisation procedure comprises three steps. In the first step, the set of candidate polynomials is sorted in preference order so that candidates with more terms are preferred over those with fewer terms. If there are multiple candidates with the same number of terms, the minimum singular value of  $\mathbf{B}$  is calculated for each candidate, and an ordering is imposed such that the candidate with the larger minimum singular value is preferred. This ordering ensures that the preferred candidate is the highest-order polynomial with the most information content.<sup>2</sup>

In the second step, the most-preferred polynomial is taken from the list of candidates and the multipliers are assigned so that the upwind cell and downwind cell have multipliers  $m_u = 2^{10}$  and  $m_d = 2^{10}$  respectively, and all peripheral points have multipliers  $m_p = 1$ . These multipliers are

---

<sup>2</sup>Note that singular values are used for two purposes: first, to test if the matrix  $\mathbf{B}$  is full-rank and, second, to impose an ordering on candidates. We have used the minimum singular value,  $\sigma_{\min}(\mathbf{B})$ , for both purposes. Alternatively, we could use the condition number,  $\text{cond}(\mathbf{B})$ , which is the ratio of smallest to largest singular value. Experiments revealed that only the candidate ordering was sensitive to the choice of  $\sigma_{\min}$  or  $\text{cond}$ . The most suitable choices of singular value calculations could be explored in future.

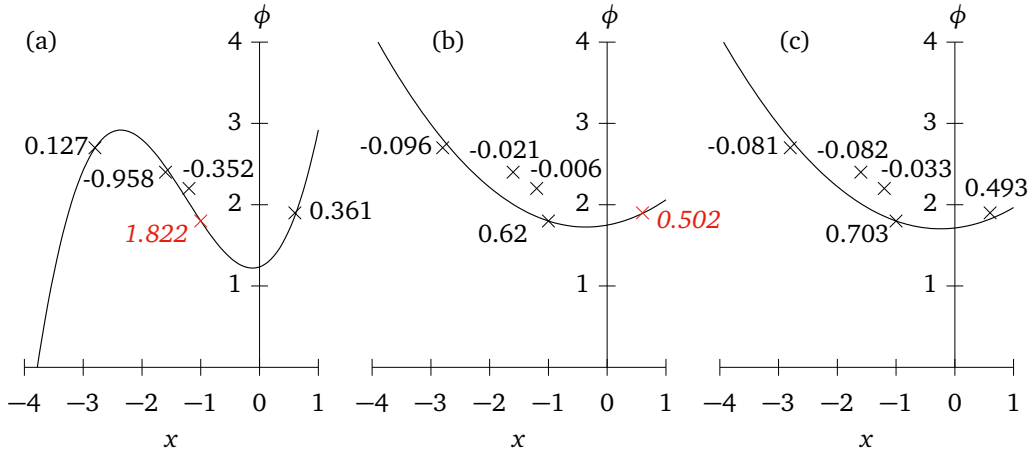


Figure 2.4: One-dimensional least-squares fits with a stencil of five points using (a) a cubic polynomial with multipliers  $m_u = 1024$ ,  $m_d = 1024$  and  $m_p = 1$ , (b) a quadratic polynomial with the same multipliers, and (c) a quadratic polynomial with multipliers  $m_u = 1024$ ,  $m_d = 1$  and  $m_p = 1$ . Notice that the curves in (a) and (b) fit almost exactly through the upwind and downwind points immediately adjacent to the  $y$ -axis, but in (c) the curve fits almost exactly only through the upwind point immediately to the left of the  $y$ -axis. The point data are labelled with their respective weights. Points that have failed one of the stability conditions in equation (2.38) are marked in red with italicised labels. The upwind point is located at  $(-1, 1.8)$  and the downwind point at  $(0.62, 1.9)$ , and the peripheral points are at  $(-2.8, 2.4)$ ,  $(-1.6, 2.7)$  and  $(-1.2, 2.2)$ . The stabilisation procedure (section 2.1) calculates weights using only  $x$  positions, and values of  $\phi$  are included here for illustration only.

very similar to those used by Lashley (2002), leading to a well-conditioned matrix  $\tilde{\mathbf{B}}$  and a least-squares fit in which the polynomial passes almost exactly through the upwind and downwind cell centre values.

In the third step, we calculate the weights  $\mathbf{w}$  and evaluate them against the stability conditions given in equation (2.38). If any condition is violated, the value of  $m_d$  is halved and the conditions are evaluated with the new weights. This step is repeated until the weights satisfy the stability conditions, or  $m_d$  becomes smaller than one. In practice, the conditions are satisfied when  $m_d$  is either small (between 1 and 4) or equal to  $2^{10}$ . The upwind multiplier  $m_u$  is fixed at  $2^{10}$  and the peripheral multipliers  $m_p$  are fixed at 1. If the conditions are still not satisfied, then we start again from the second step with the next polynomial in the candidate list.

Finally, if no stable weights are found for any candidate polynomial, we revert to an upwind scheme such that  $w_u = 1$  and all other weights are zero. In our experiments we have not encountered any stencil for which this last resort is required. Furthermore, our experiments show that the stabilisation procedure only modifies the least squares fit for stencils near boundaries and for stencils in distorted mesh regions. For stencils in the interior of a uniform rectangular mesh, the least squares fit includes all terms in equation (2.5) with  $m_u = m_d = 2^{10}$ .

To illustrate the stabilisation procedure, figure 2.4a presents a one-dimensional example of a cubic polynomial fitted through five points, with the weight at each point printed beside it. The

stabilisation procedure only uses the  $x$  positions of these points and does not use the values of  $\phi$  themselves. The  $\phi$  values are included here for illustration only. Hence, for a given set of  $x$  positions, the same set of weights are chosen irrespective of the  $\phi$  values.

For a one-dimensional cubic polynomial fit, the list of candidate polynomials in preference order is

$$\phi = a_1 + a_2x + a_3x^2 + a_4x^3 , \quad (2.39)$$

$$\phi = a_1 + a_2x + a_3x^2 , \quad (2.40)$$

$$\phi = a_1 + a_2x , \quad (2.41)$$

$$\phi = a_1 . \quad (2.42)$$

We begin with the cubic equation (2.39). The multipliers are chosen so that the polynomial passes almost exactly through the upwind and downwind points that are immediately to the left and right of the  $y$ -axis respectively. The stability condition on the upwind point is violated because  $w_u = 1.822 > 1$  (equation 2.38a). Reducing the downwind multiplier does not help to satisfy the stability condition, so we start again with the quadratic equation (2.40), and the new fit is presented in figure 2.4b. Again, the multipliers are chosen to force the polynomial through the upwind and downwind points, but this violates the stability condition on the downwind point because  $w_d = 0.502 > 0.5$  (equation 2.38b). This time, however, stable weights are found by reducing  $m_d$  to one (figure 2.4c) and these are the weights that will be used to approximate  $\phi_F$ , where the polynomial intercepts the  $y$ -axis.

### Future extension to three dimensions

All the procedures used in the cubicFit scheme generalise to three dimensions. The stencil construction procedure described in section 2.1 creates a stencil with 12 cells for a face in the interior of a two-dimensional rectangular mesh. In three dimensions, the same procedure creates a stencil with  $3 \times 12 = 36$  cells. A three-dimensional stencil has three times as many cells as its two-dimensional counterpart if the mesh has prismatic cells arranged in columns. Hence, the computational cost during integration increases three-fold when moving from two dimensions to three dimensions.

To extend the least squares fit to three dimensions, the two-dimensional polynomial in equation (2.5) is replaced with its three-dimensional counterpart,

$$\begin{aligned} \phi = & a_1 + a_2x + a_3y + a_4z + a_5x^2 + a_6xy + a_7y^2 + a_8xz + a_9yz + a_{10}z^2 + \\ & a_{11}x^3 + a_{12}x^2y + a_{13}xy^2 + a_{14}x^2z + a_{15}xz^2 + a_{16}yz^2 + a_{17}y^2z + a_{18}xyz . \end{aligned} \quad (2.43)$$

The procedure for generating candidate polynomials described in section 2.1 results in 26 dense subsets in two dimensions and 842 dense subsets in three dimensions. Note that the combinatorial explosion of dense subsets in three dimensions does not increase the computational cost during integration.

The stabilisation procedure described in section 2.1 requires further numerical experiments to verify that it is sufficient for three-dimensional flows and arbitrary polyhedral meshes. An initial three-dimensional test with uniform flow and a uniform Cartesian mesh obtained a numerically stable result. For stencils in the interior of the domain, the least squares fit includes all polynomial terms in equation (2.43) with  $m_u = m_d = 2^{10}$ . The stabilisation procedure does not modify the least squares fit for these stencils, but we have not explored the three-dimensional extension of cubicFit any further.

### Multidimensional linear upwind transport scheme

The multidimensional linear upwind scheme, called “linearUpwind” hereafter, is documented here since it provides a baseline accuracy for the experiments that follow. The approximation of  $\phi_F$  is calculated using a gradient reconstruction,

$$\phi_F = \phi_u + \nabla_c \phi \cdot (\mathbf{x}_f - \mathbf{x}_c) \quad (2.44)$$

where  $\phi_u$  is the upwind value of  $\phi$ , and  $\mathbf{x}_f$  and  $\mathbf{x}_c$  are the position vectors of the face centroid and cell centroid respectively. The gradient  $\nabla_c \phi$  is calculated using Gauss’ theorem:

$$\nabla_c \phi = \frac{1}{\mathcal{V}_c} \sum_{f \in c} \tilde{\phi}_F \mathbf{s}_f \quad (2.45)$$

where  $\tilde{\phi}_F$  is linearly interpolated from the two neighbouring cells of face  $f$ . The resulting stencil comprises all cells sharing a face with the upwind cell, including the upwind cell itself. For a face in the interior of a two-dimensional rectangular mesh, the stencil for the linearUpwind scheme is a ‘+’ shape with 5 cells. On the same mesh, the stencil for the cubicFit scheme is more than twice the size with 12 cells. For cells adjacent to boundaries having zero gradient boundary conditions, the boundary value is set to be equal to the cell centre value before equation (2.45) is evaluated. This implementation of the multidimensional linear upwind scheme is included in the OpenFOAM software distribution ([CFD Direct, 2016](#)).

## 2.2 Horizontal transport over mountains

A two-dimensional transport test was developed by [Schär et al. \(2002\)](#) to study the effect of terrain-following coordinate transformations on numerical accuracy. In this standard test, a tracer is positioned aloft and transported horizontally over wave-shaped mountains. When terrain-following meshes are used, this test challenges transport schemes because the tracer must cross mesh layers, which acts to reduce numerical accuracy ([Schär et al., 2002](#)). Here we use a more challenging variant of the test that has steeper mountains and highly-distorted terrain-following meshes. Numerical convergence and numerical error structures are compared using the linearUpwind and cubicFit transport schemes on terrain-following meshes and cut cell meshes.

The domain is defined on a rectangular  $x$ - $z$  plane that is 300 km wide as measured between the outermost cell centres, and 25 km high as measured between upper and lower boundary edges. Boundary conditions are imposed on the tracer density  $\phi$  such that  $\phi = 0 \text{ kg m}^{-3}$  at the inlet boundary, and a zero normal gradient  $\partial\phi/\partial n = 0 \text{ kg m}^{-4}$  is imposed at the outlet boundary. There is no normal flow at the lower and upper boundaries.

The terrain is wave-shaped, specified by the surface elevation  $h$  such that

$$h(x) = h^* \cos^2(\alpha x) \quad (2.46a)$$

where

$$h^*(x) = \begin{cases} h_0 \cos^2(\beta x) & \text{if } |x| < a \\ 0 & \text{otherwise} \end{cases} \quad (2.46b)$$

where  $a = 25 \text{ km}$  is the mountain envelope half-width,  $h_0 = 6 \text{ km}$  is the maximum mountain height,  $\lambda = 8 \text{ km}$  is the wavelength,  $\alpha = \pi/\lambda$  and  $\beta = \pi/(2a)$ . Note that, in order to make this test more challenging, the mountain height  $h_0$  is double the mountain height used by [Schär et al. \(2002\)](#).

*TODO: might have already described BTF in a previous chapter* A basic terrain-following (BTF) mesh is constructed by using the terrain profile to modify the uniform mesh. The BTF method uses a linear decay function so that mesh layers become horizontal at the top of the model domain ([Gal-Chen and Somerville, 1975](#)),

$$z(x) = (H - h(x))(z^*/H) + h(x) \quad (2.47)$$

where  $z$  is the geometric height,  $H$  is the height of the domain,  $h(x)$  is the surface elevation and  $z^*$  is the computational height of a mesh layer. If there were no terrain then  $h = 0$  and  $z = z^*$ .

A velocity field is prescribed with uniform horizontal flow aloft and zero flow near the ground,

$$u(z) = u_0 \begin{cases} 1 & \text{if } z \geq z_2 \\ \sin^2\left(\frac{\pi}{2} \frac{z-z_1}{z_2-z_1}\right) & \text{if } z_1 < z < z_2 \\ 0 & \text{otherwise} \end{cases} \quad (2.48)$$

where  $u_0 = 10 \text{ m s}^{-1}$ ,  $z_1 = 7 \text{ km}$  and  $z_2 = 8 \text{ km}$ . This results in a constant wind above  $z_2$ , and zero flow at 7 km and below.

The discrete velocity field is defined using a streamfunction,  $\Psi$ . Given that  $u = -\partial\Psi/\partial z$ , the streamfunction is found by vertical integration of the velocity profile:

$$\Psi(z) = -\frac{u_0}{2} \begin{cases} (2z - z_1 - z_2) & \text{if } z > z_2 \\ z - z_1 - \frac{z_2 - z_1}{\pi} \sin\left(\pi \frac{z-z_1}{z_2-z_1}\right) & \text{if } z_1 < z \leq z_2 \\ 0 & \text{if } z \leq z_1 \end{cases} \quad (2.49)$$

A tracer with density  $\phi$  is positioned upstream above the height of the terrain. It has the shape

$$\phi(x, z) = \phi_0 \begin{cases} \cos^2\left(\frac{\pi r}{2}\right) & \text{if } r \leq 1 \\ 0 & \text{otherwise} \end{cases} \quad (2.50a)$$

with radius  $r$  given by

$$r = \sqrt{\left(\frac{x-x_0}{A_x}\right)^2 + \left(\frac{z-z_0}{A_z}\right)^2} \quad (2.50b)$$

where  $A_x = 25\text{ km}$ ,  $A_z = 3\text{ km}$  are the horizontal and vertical half-widths respectively, and  $\phi_0 = 1\text{ kg m}^{-3}$  is the maximum density of the tracer. At  $t = 0\text{ s}$ , the tracer is centred at  $(x_0, z_0) = (-50\text{ km}, 12\text{ km})$  so that the tracer is upwind of the mountain, in the region of uniform flow above  $z_2$ .

Tests are integrated for 10 000 s using  $\Delta t$  chosen for each mesh so that the maximum Courant number is about 0.4. This choice yields a time-step that is well below any stability limit, as recommended by [Lauritzen et al. \(2012\)](#). By the end of integration the tracer is positioned downwind of the mountain. The analytic solution at  $t = 10 000\text{ s}$  is centred at  $(x_0, z_0) = (50\text{ km}, 12\text{ km})$  with its shape unchanged from the initial condition.

To assess numerical convergence, a range of mesh spacings are chosen so that  $\Delta x : \Delta z = 2 : 1$  to match the original test specification from [Schär et al. \(2002\)](#). Tests were performed using the linearUpwind and cubicFit schemes using BTF meshes and cut cell meshes with mesh spacings between  $\Delta x = 250\text{ m}$  and  $\Delta x = 5000\text{ m}$ . Error norms are calculated by subtracting the analytic solution from the numerical solution,

$$\ell_2 = \sqrt{\frac{\sum_c (\phi - \phi_T)^2 \gamma_c}{\sum_c (\phi_T^2 \gamma_c)}} \quad (2.51)$$

$$\ell_\infty = \frac{\max_c |\phi - \phi_T|}{\max_c |\phi_T|} \quad (2.52)$$

where  $\phi$  is the numerical value,  $\phi_T$  is the analytic value,  $\sum_c$  denotes a summation over all cells  $c$  in the domain, and  $\max_c$  denotes a maximum value of any cell. The linearUpwind and cubicFit schemes are second-order convergent in the  $\ell_2$  norm (figure 2.5a) and  $\ell_\infty$  norm (figure 2.5) at all but the coarsest mesh spacings where errors are saturated for both schemes.

The cubicFit scheme achieves a given  $\ell_2$  error using a mesh spacing that is almost twice as coarse as that needed by the linearUpwind scheme. Doubling the mesh spacing results in a coarser mesh with four times fewer cells because the  $\Delta x : \Delta z$  aspect ratio is fixed. Recall that the stencil for the cubicFit scheme has about twice as many cells as the stencil for the linearUpwind scheme. Hence, for a given  $\ell_2$  error, the computational cost during integration of the cubicFit scheme is about half the computational cost of the linearUpwind scheme.

Next, we examine the structure of numerical errors with test results using the linearUpwind and cubicFit transport schemes on BTF and cut cell meshes with  $\Delta x = 1000\text{ m}$  and  $\Delta z = 500\text{ m}$ . To obtain a maximum Courant number of about 0.4, we choose  $\Delta t = 40\text{ s}$  on the cut cell mesh where the flow is aligned with mesh layers and there are no fluxes through upper and lower cell faces. Since there is no flow below  $z = 7\text{ km}$ , the time-step is not constrained by small, cut cells next to the lower boundary. On the BTF mesh,  $\Delta t$  is only 8 s because the flow is misaligned with mesh layers, with fluxes through all four faces of cells above sloping terrain.

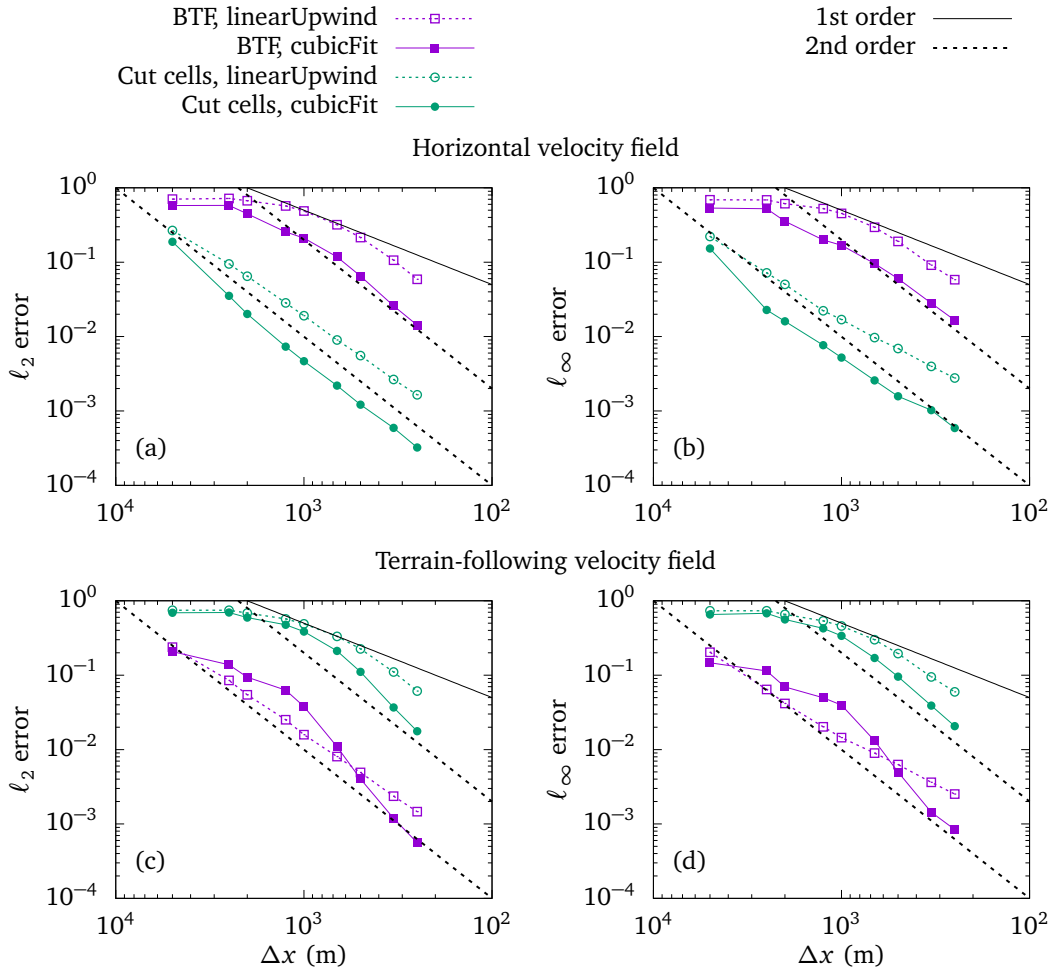


Figure 2.5: Numerical convergence of the two-dimensional tracer transport tests over mountains using (a, b) horizontal and (c, d) terrain-following velocity fields.  $\ell_2$  errors (equation 2.51) and  $\ell_\infty$  errors (equation 2.52) are marked at mesh spacings between 5000 m and 250 m using linearUpwind and cubicFit transport schemes on basic terrain-following and cut cell meshes.

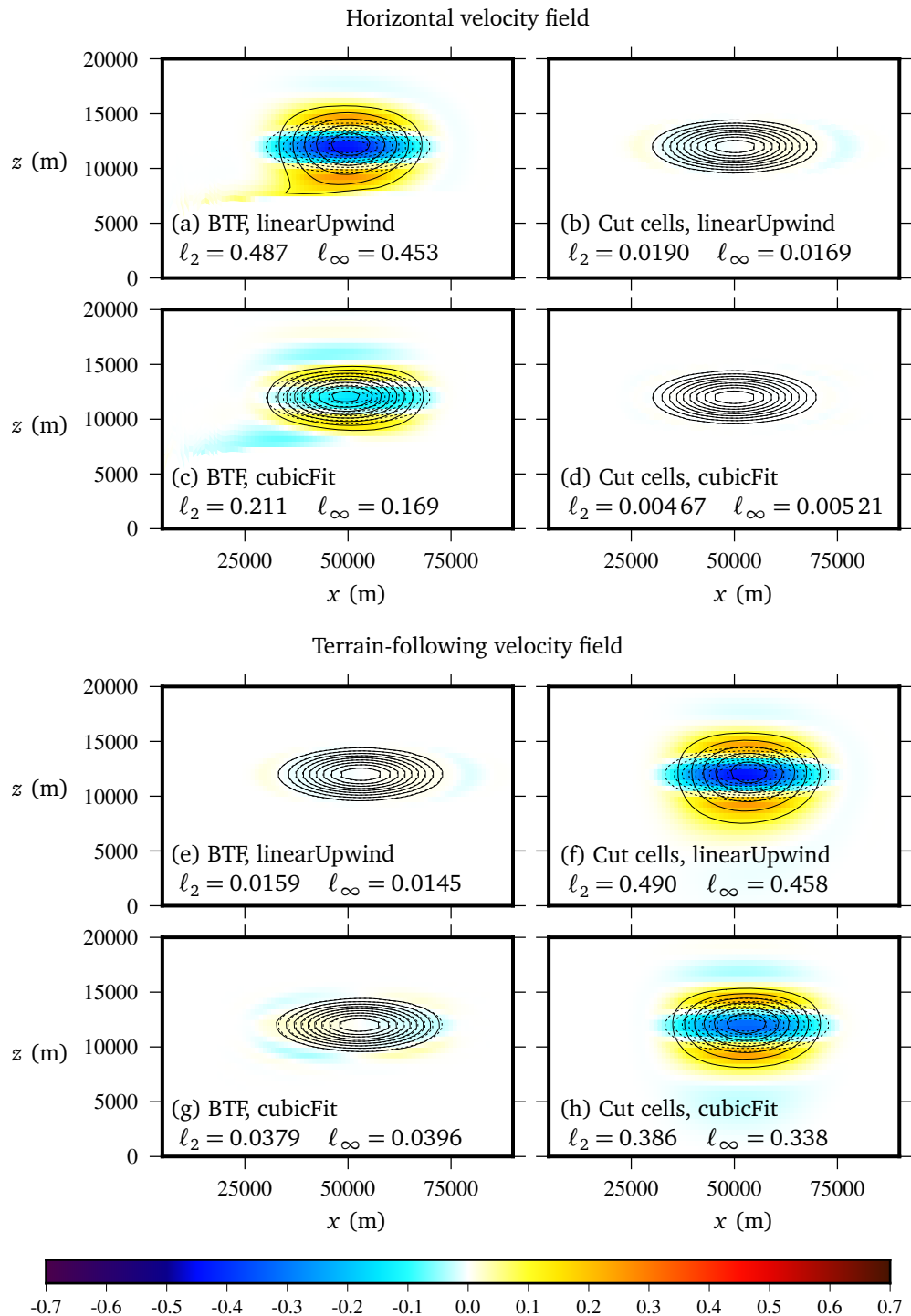


Figure 2.6: Tracer contours at the end of integration for the two-dimensional tracer transport tests over mountains using (a, b, c, d) horizontal and (e, f, g, h) terrain-following velocity fields. The numerical solution, marked with solid lines, and the analytic solution, marked with dashed lines, are plotted every 0.1. Tracer contours overlay a color error field, calculated by subtracting the analytic solution from the numerical solution. Only the lowest 20 km in the lee of the mountain is plotted. The entire domain is 301 km wide and 25 km high.

The highly-distorted BTF mesh presents a particular challenge to the linearUpwind scheme with the final numerical solution, marked by solid lines, losing its correct shape and maximum intensity compared to the analytic solution marked by dashed lines (figure 2.6a). The linearUpwind scheme produces a much better solution on the cut cell mesh, with only small phase errors apparent in figure 2.6b. Accuracy is much improved using the cubicFit scheme: on the BTF mesh, shape and maximum intensity are similar to the analytic solution (figure 2.6c) and, on the cut cell mesh, numerical errors are so small they are not visible (figure 2.6d). The numerical and analytic contours overlay a color error field that reveals horizontal streaks of error on the BTF mesh (figure 2.6a, 2.6c) that were generated above the steepest mountain peaks before becoming trapped in the region of zero flow below  $z = 7\text{ km}$ .

The horizontal transport test demonstrates that the cubicFit scheme is second-order convergent in the domain interior irrespective of mesh distortions. Numerical errors are largest on terrain-following meshes, due either to misalignment of the flow with mesh layers, or to mesh distortions. In the next section, we propose a new test in order to identify the primary cause of these numerical errors.

### 2.3 Transport in a terrain-following velocity field

In the horizontal transport test, results were least accurate on the BTF mesh where the mesh was most distorted and flow was misaligned with mesh layers. Here, we formulate a new tracer transport test in which the velocity field is everywhere tangential to the basic terrain-following mesh layers. The flow is then aligned with the BTF mesh layers, but the points in the linearUpwind and cubicFit stencils are not uniformly distributed because the BTF mesh is distorted. Conversely, the flow is misaligned with the cut cell mesh layers but, except in cut cells next to the ground, the cut cell mesh is undistorted. This test determines whether the primary source of numerical error is due to mesh distortions or misalignment of the flow with mesh layers.

The domain size, mountain profile, initial tracer profile and boundary conditions are the same as those in the horizontal tracer advection test in section 2.2. The discrete velocity field is calculated using a streamfunction  $\Psi$  in the same way as the horizontal transport test. Here, we define a different streamfunction that yields a velocity field that follows the BTF mesh layers given by equation (2.47) such that

$$\Psi(x, z) = -u_0 H_1 \frac{z - h}{H_1 - h} \quad (2.53)$$

where  $u_0 = 10\text{ m s}^{-1}$ , which is the horizontal velocity where  $h(x) = 0$ . The velocity field follows the lower boundary and becomes entirely horizontal at  $H_1 = H = 25\text{ km}$ , hence, there is no normal flow at the lower and upper boundaries. In the domain interior, the flow is predominantly horizontal, with non-zero vertical velocities only above sloping terrain.

The horizontal and vertical components of velocity,  $u$  and  $w$ , are given by

$$u = -\frac{\partial \Psi}{\partial z} = u_0 \frac{H_1}{H_1 - h}, \quad w = \frac{\partial \Psi}{\partial x} = u_0 H_1 \frac{dh}{dx} \frac{H_1 - z}{(H_1 - h)^2}, \quad (2.54)$$

$$\frac{dh}{dx} = -h_0 [\beta \cos^2(\alpha x) \sin(2\beta x) + \alpha \cos^2(\beta x) \sin(2\alpha x)]. \quad (2.55)$$

Unlike the horizontal transport test, the velocity field presented here extends from the top of the domain all the way to the ground.

An analytic solution at 10 000 s is obtained by calculating the new horizontal position of the tracer. Integrating along the trajectory yields  $t$ , the time taken to move from the left side of the mountain at  $-a$ , to the right side of the mountain at  $a$ ,

$$dt = dx/u(x) \quad (2.56)$$

$$t = \int_{-a}^a \frac{H_1 - h(x)}{u_0 H_1} dx \quad (2.57)$$

$$t = \frac{2a}{u_0} - \frac{h_0}{16u_0 H_1} \left[ 4x + \frac{\sin 2(\alpha + \beta)x}{\alpha + \beta} + \frac{\sin 2(\alpha - \beta)x}{\alpha - \beta} + 2 \left( \frac{\sin 2\alpha x}{\alpha} + \frac{\sin 2\beta x}{\beta} \right) \right]_{-a}^a \quad (2.58)$$

Because the velocity field is non-divergent, the flow accelerates over mountain ridges and the tracer travels **TODO: 123 m** further compared to the tracer in a purely horizontal velocity field. The vertical tracer position is unchanged downwind of the mountains because flow is parallel to the mesh layers.

To enable comparisons with the horizontal transport test, results are obtained using the linearUpwind and cubicFit transport schemes on BTF and cut cell meshes with  $\Delta x = 1000$  m and  $\Delta z = 500$  m. To obtain a maximum Courant number of about 0.4, we choose  $\Delta t = 25$  s on the BTF mesh where flow is aligned with mesh layers. The cut cell mesh suffers from the small cell problem, having a more stringent time-step constraint of  $\Delta t = 8$  s. Recall that, in this test, there is flow everywhere in the domain, and it is flow through arbitrarily small cut cells that imposes the more stringent time-step constraint.

Figure 2.7 shows results using the cubicFit scheme on the BTF mesh, illustrating the evolution of the tracer with snapshots plotted every 5000 s. At  $t = 5000$  s, the tracer is distorted by the terrain-following velocity field but, by  $t = 10 000$  s, the tracer has correctly returned to its original shape, with some phase errors apparent when comparing the numerical solution (solid contours) with the analytic solution (dashed contours). The region highlighted in orange corresponds to the region plotted in figure 2.6, where tracer contours and numerical errors are plotted at  $t = 10 000$  s.

Unlike the horizontal transport test, results are most accurate on the BTF mesh (linearUpwind, figure 2.6e; cubicFit, figure 2.6g) and least accurate on the cut cell mesh (linearUpwind, figure 2.6f; cubicFit, figure 2.6h). Hence, we conclude that the accuracy of the transport schemes depends upon alignment of the flow with mesh layers, and accuracy is mostly unaffected by mesh distortions. The error structures on the cut cell mesh in this test (2.6f, 2.6h) are similar to the error structures on the BTF mesh in the horizontal transport test (2.6a, 2.6c), and the phase

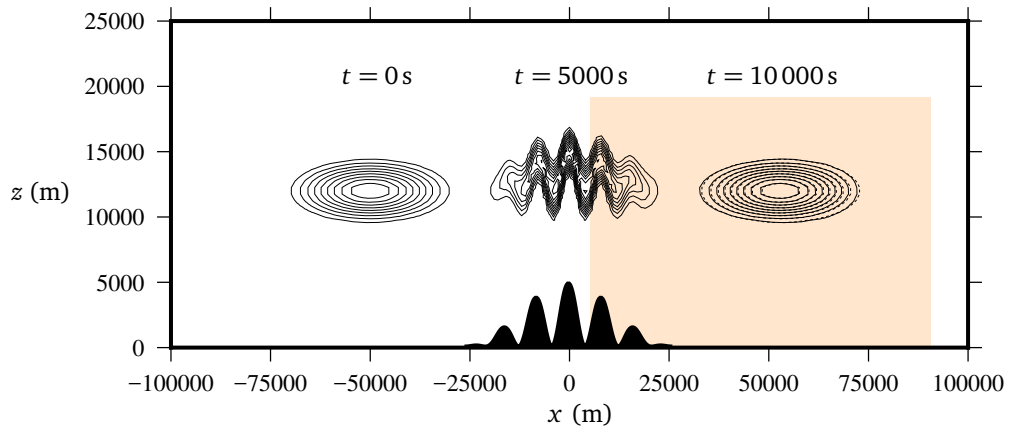


Figure 2.7: Tracer contours transported above mountains in a terrain-following velocity field at  $t = 0\text{ s}$ ,  $5000\text{ s}$ , and  $10\,000\text{ s}$  using the cubicFit transport scheme on a BTF mesh. The analytic solution at  $t = 10\,000\text{ s}$  is plotted with dashed contours. All contour intervals are  $0.1$ . The terrain profile is shown immediately above the  $x$  axis. The region highlighted in orange marks the region plotted in the panels of figure 2.6. Only the central  $200\text{ km}$  of the domain is shown. The entire domain is  $301\text{ km}$  wide and  $25\text{ km}$  high.

error using the linearUpwind scheme on the BTF mesh (2.6e) closely resembles the error on the cut cell mesh in the horizontal transport test (2.6b).

Perhaps surprisingly, errors are slightly larger using the cubicFit scheme on the BTF mesh (2.6g) compared to those obtained using the linearUpwind scheme (2.6e). *TODO: can we conjecture a reason?* At finer mesh spacings, however, cubicFit is more accurate on BTF and cut cell meshes in both the  $\ell_2$  norm (figure 2.5c) and  $\ell_\infty$  norm (figure 2.5d). Once again, both transport schemes are second-order convergent irrespective of mesh distortions or misalignment of the flow with mesh layers.

In both horizontal and terrain-following transport tests, which are both variations on the standard test case by Schär et al. (2002), the linearUpwind and cubicFit transport schemes are second-order convergent irrespective of mesh distortions or misalignment of the flow with mesh layers. Together, the horizontal and terrain-following transport tests demonstrate that numerical accuracy depends primarily on the alignment of the flow with mesh layers.

## 2.4 Deformational flow on a sphere

The tests presented so far have used flows that are mostly uniform on meshes that are based on rectangular cells. To ensure that the cubicFit transport scheme is suitable for complex flows on a variety of meshes, we use a standard test of deformational flow on a spherical Earth, as specified by Lauritzen et al. (2012). Results are compared between linearUpwind and cubicFit schemes using hexagonal-icosahedral meshes and cubed-sphere meshes. Hexagonal-icosahedral meshes are constructed by successive refinement of a regular icosahedron following the approach by

[Thuburn et al. \(2014\)](#); [Heikes and Randall \(1995a,b\)](#) without any mesh twisting. Cubed-sphere meshes are constructed using an equi-distant gnomic projection of a cube having a uniform Cartesian mesh on each panel ([Staniforth and Thuburn, 2012](#)).

Following appendix A9 in [Lauritzen et al. \(2014\)](#), the average equatorial spacing  $\Delta\lambda$  is used as a measure of mesh spacing. It is defined as

$$\Delta\lambda = 360^\circ \frac{\overline{\Delta x}}{2\pi R_e} \quad (2.59)$$

where  $\overline{\Delta x}$  is the mean distance between cell centres and  $R_e = 6.3712 \times 10^6$  m is the radius of the Earth.

The deformational flow test specified by [Lauritzen et al. \(2012\)](#) comprised six elements:

1. a convergence test using a Gaussian-shaped tracer
2. a “minimal” resolution test using a cosine bell-shaped tracer
3. a test of filament preservation
4. a test using a “rough” slotted cylinder tracer
5. a test of correlation preservation between two tracers
6. a test using a divergent velocity field

We assess the cubicFit scheme using the first two tests only. We do not consider filament preservation, correlation preservation, or the transport of a “rough” slotted cylinder because no shape-preserving filter has yet been developed for the cubicFit scheme. Stable results were obtained when testing the cubicFit scheme using a divergent velocity field, but no further analysis is made here.

The first deformational flow test uses an infinitely continuous initial tracer that is transported in a non-divergent, time-varying, rotational velocity field. The velocity field deforms two Gaussian ‘hills’ of tracer into thin vortical filaments. Half-way through the integration the rotation reverses so that the filaments become circular hills once again. The analytic solution at the end of integration is identical to the initial condition. A rotational flow is superimposed on a time-invariant background flow in order to avoid error cancellation. The non-divergent velocity field is defined by the streamfunction  $\Psi$ ,

$$\Psi(\lambda, \theta, t) = \frac{10R_e}{T} \sin^2(\lambda') \cos^2(\theta) \cos\left(\frac{\pi t}{T}\right) - \frac{2\pi R_e}{T} \sin(\theta) \quad (2.60)$$

where  $\lambda$  is a longitude,  $\theta$  is a latitude,  $\lambda' = \lambda - 2\pi t/T$ , and  $T = 12$  days is the duration of integration. The time-step is chosen such that the maximum Courant number is about 0.4.

The initial tracer density  $\phi$  is defined as the sum of two Gaussian hills,

$$\phi = \phi_1(\lambda, \theta) + \phi_2(\lambda, \theta). \quad (2.61)$$

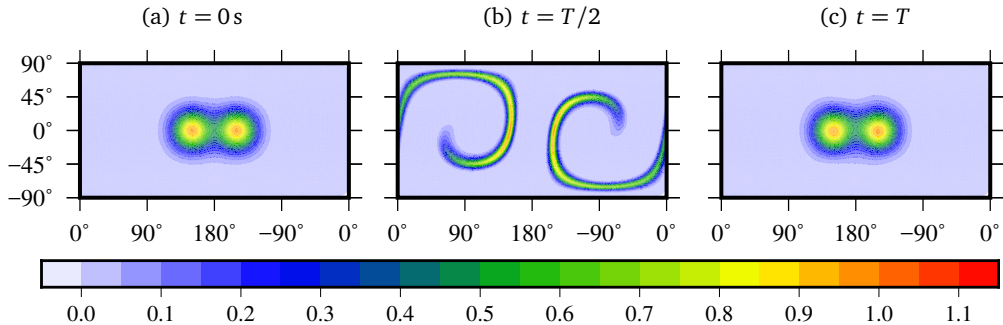


Figure 2.8: Tracer fields for the deformational flow test using initial Gaussian hills. The tracer is deformed by the velocity field before the rotation reverses to return the tracer to its original distribution: (a) the initial tracer distribution at  $t = 0\text{ s}$ ; (b) by  $t = T/2$  the Gaussian hills are stretched into a thin S-shaped filament; (c) at  $t = T$  the tracer resembles the initial Gaussian hills except for some distortion and diffusion due to numerical errors. Results were obtained with the cubicFit scheme on a hexagonal-icosahedral mesh with an average equatorial mesh spacing of  $\Delta\lambda = 16.9^\circ$ .

An individual hill  $\phi_i$  is given by

$$\phi_i(\lambda, \theta) = \phi_0 \exp\left(-b \left(\frac{|\mathbf{x} - \mathbf{x}_i|}{R_e}\right)^2\right) \quad (2.62)$$

where  $\phi_0 = 0.95\text{ kg m}^{-3}$  and  $b = 5$ . The Cartesian position vector  $\mathbf{x} = (x, y, z)$  is related to the spherical coordinates  $(\lambda, \theta)$  by

$$(x, y, z) = (R_e \cos \theta \cos \lambda, R_e \cos \theta \sin \lambda, R_e \sin \theta). \quad (2.63)$$

The centre of hill  $i$  is positioned at  $\mathbf{x}_i$ . In spherical coordinates, two hills are centred at

$$(\lambda_1, \theta_1) = (5\pi/6, 0) \quad (2.64)$$

$$(\lambda_2, \theta_2) = (7\pi/6, 0) \quad (2.65)$$

The results in figure 2.8 are obtained using the cubicFit scheme on a hexagonal-icosahedral mesh with  $\Delta\lambda = 16.9^\circ$ . The initial Gaussian hills are shown in figure 2.8a. At  $t = T/2$  the tracer has been deformed into an S-shaped filament (figure 2.8b). By  $t = T$  the tracer has almost returned to its original distribution except for some slight distortion and diffusion that are the result of numerical errors (figure 2.8c).

To determine the order of convergence and relative accuracy of the linearUpwind and cubicFit schemes, the same test was performed at a variety of mesh spacings between  $\Delta\lambda = 8.61^\circ$  and  $\Delta\lambda = 16.9^\circ$  on hexagonal-icosahedral meshes and cubed-sphere meshes. The results are shown in figure 2.9. The solution is slow to converge at coarse resolutions, and this behaviour agrees with the results from Lauritzen et al. (2012). Both linearUpwind and cubicFit schemes achieve second-order accuracy at smaller mesh spacings. For any given mesh type and mesh spacing, the cubicFit scheme is more accurate than the linearUpwind scheme. Results are more accurate

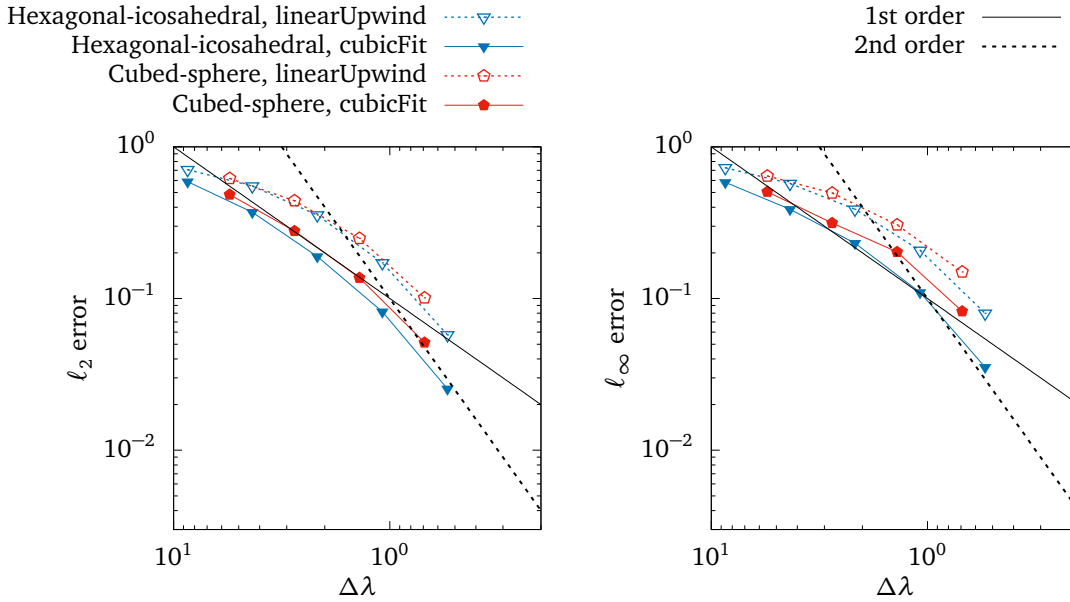


Figure 2.9: Numerical convergence of the deformational flow test on the sphere using initial Gaussian hills.  $\ell_2$  errors (equation 2.51) and  $\ell_\infty$  errors (equation 2.52) are marked at mesh spacings between  $8.61^\circ$  and  $16.9^\circ$  using the linearUpwind scheme (dotted lines) and the cubicFit scheme (solid lines) on hexagonal-icosahedral meshes and cubed-sphere meshes.

using hexagonal-icosahedral meshes compared to cubed-sphere meshes. It is not known whether the larger errors on cubed-sphere meshes are due to mesh non-uniformities at panel corners but there is no evidence of grid imprinting in the error fields (not shown).

A slightly more challenging variant of the same test is performed using a quasi-smooth tracer field defined as the sum of two cosine bells,

$$\phi = \begin{cases} b + c\phi_1(\lambda, \theta) & \text{if } r_1 < r, \\ b + c\phi_2(\lambda, \theta) & \text{if } r_2 < r, \\ b & \text{otherwise.} \end{cases} \quad (2.66)$$

The velocity field is the same as before. This test is used to determine the “minimal” resolution,  $\Delta\lambda_m$ , which is specified by [Lauritzen et al. \(2012\)](#) as the coarsest mesh spacing for which  $\ell_2 \approx 0.033$ .

The minimal resolution for the cubicFit scheme on a hexagonal-icosahedral mesh is about  $\Delta\lambda_m = 0.3^\circ$ . Tests were not performed at mesh spacings finer than  $\Delta\lambda = 16.9^\circ$  but approximate minimal resolutions have been extrapolated from the second-order convergence that is found at fine mesh spacings. These minimal resolutions are presented in table 2.1 along with a selection of transport schemes having similar minimal resolutions from the model intercomparison by [Lauritzen et al. \(2014\)](#).

The series of deformational flow tests presented here demonstrate that the cubicFit scheme

Transport scheme	Mesh type	Minimal resolution ( $^{\circ}$ )
linearUpwind	Cubed-sphere	0.15
FARSIGHT, grid-point semi-Lagrangian <i>(White and Dongarra, 2011)</i>	Cubed-sphere	0.1875
linearUpwind	Hexagonal-icosahedral	0.2
SLFV-SL, swept-area scheme <i>(Miura, 2007)</i>	Hexagonal-icosahedral	0.25
cubicFit	Cubed-sphere	0.25
cubicFit	Hexagonal-icosahedral	0.3
ICON-FFSL, swept-area scheme <i>(Miura, 2007)</i>	Triangular-icosahedral	0.42

Table 2.1: Minimal resolutions for the cubicFit and linearUpwind schemes in the test of deformational flow using cosine bells. Italicised values have been extrapolated using the second-order convergence obtained at coarser mesh spacings. For comparison with existing models, some results are also included for unlimited versions of the transport schemes from the intercomparison by [Lauritzen et al. \(2014\)](#).

is suitable for transport on spherical meshes based on quadrilaterals and hexagons. The cubicFit scheme is largely insensitive to the mesh type, and results are more accurate compared to the linearUpwind scheme for a given mesh type and mesh spacing. Neither scheme requires special treatment at the corners of cubed-sphere panels.

### 3 A new mesh for representing the atmosphere above terrain

---

#### Highlights

- The new slanted cell mesh permits longer time-steps than cut cells, with time-steps comparable to terrain-following meshes
  - Pressure gradient calculations are more accurate using the new slanted cell method compared to terrain-following methods
  - Unlike the multidimensional linear upwind scheme, the cubicFit scheme is numerically stable over very steep slopes
- 

Two sources of numerical error receive particular attention in atmospheric models: errors associated with transport terms and errors associated with the pressure gradient term. The previous chapter developed the cubicFit transport scheme that reduces numerical errors associated with transport over mountains. This chapter seeks to reduce errors associated with pressure gradient calculations by representing the atmosphere above terrain using a new type of mesh, the slanted cell mesh.

Pressure gradient errors result in spurious flows that are especially apparent for diurnal valley flows where synoptic-scale winds are weak (Fast, 2003), and even small velocity errors can produce large errors in derived quantities such as relative vorticity and potential vorticity (Hoinka and Zängl, 2004). These numerical errors are particularly large using terrain-following meshes with steeply sloping terrain (Zängl, 2012). Terrain-following meshes are typically implemented using a coordinate transform that introduces metric terms into the equations of motion. The horizontal pressure gradient  $\partial p / \partial x|_z$  can be written as (Mahrer, 1984)

$$\frac{\partial p}{\partial x} \Big|_z = \frac{\partial p}{\partial x} \Big|_{z^*} + \frac{\partial z^*}{\partial x} \Big|_z \frac{\partial p}{\partial z^*} \quad (3.1)$$

where  $\partial / \partial x|_z$  denotes a horizontal derivative at a fixed height in the physical domain, and

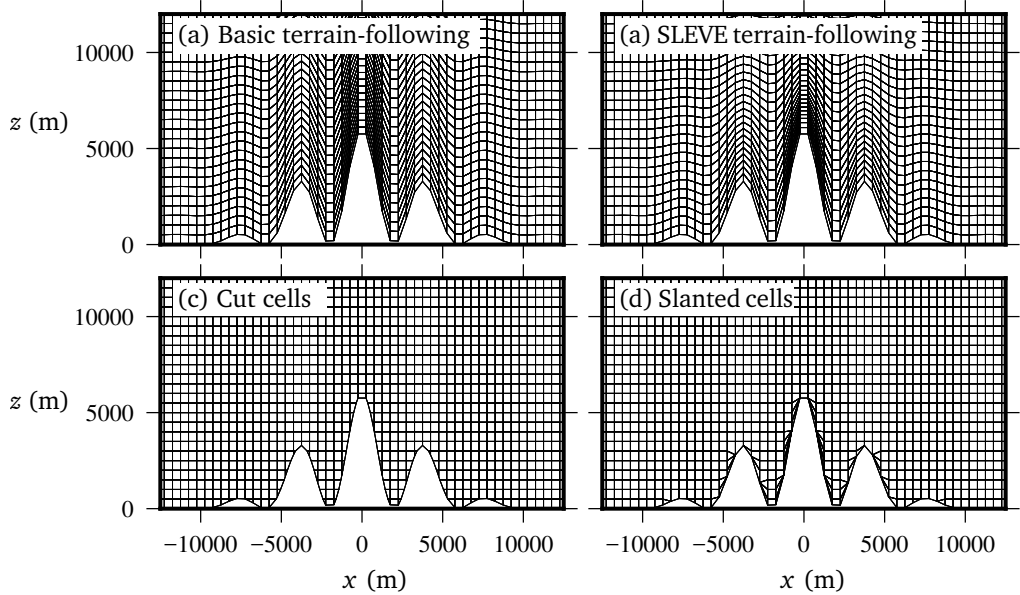


Figure 3.1: Two dimensional  $x$ - $z$  meshes created with the (a) basic terrain-following, (b) SLEVE, (c) cut cell, and (d) slanted cell methods, used for the resting atmosphere tests in section 3.4. Cell edges are marked by thin black lines. The peak mountain height  $h_0 = 6$  km. Only the lowest 12 km for the central region of the domain is shown. The entire domain is 201 km wide and 20 km high.

$\partial/\partial x|_{z^*}$  denotes a horizontal derivative at a fixed model level in the computational domain. The first term on the right hand side of equation (3.1) is the change in pressure along the terrain-following coordinate surfacee, and the second term corrects for the vertical contribution in the first. These terms tend to be large and of opposite sign over steep terrain, and cancellation errors between the two terms result in pressure gradients errors that drive spurious flows.

There are two common approaches to reducing errors associated with terrain-following meshes. The first approach reduces the influence of the terrain on the mesh by choosing a vertical decay function that smooths mesh layers rapidly with height. The Smooth Level Vertical (SLEVE) decay function formulated by Schär et al. (2002), later improved by Leuenberger et al. (2010), is one such approach. The SLEVE method achieves a less distorted terrain-following mesh in the middle and top of the domain than the BTF method. The difference is illustrated in figure 3.1, in which the SLEVE mesh (figure 3.1b) is noticeably smoother than the equivalent BTF mesh (figure 3.1a). The terrain height is split into coarse-scale and fine-scale components,  $h_1$  and  $h_2$ , such that  $h = h_1 + h_2$ , with each component having a different exponential decay. The transformation is defined as (Leuenberger et al., 2010)

$$z = z^* + h_1 b_1 + h_2 b_2 \quad (3.2)$$

where the vertical decay functions are given by

$$b_i = \frac{\sinh((H/s_i)^n - (z^*/s_i)^n)}{\sinh(H/s_i)^n} \quad (3.3)$$

and  $s_1$  and  $s_2$  are the scale heights of coarse-scale and fine-scale terrain respectively. The exponent  $n$  was introduced by [Leuenberger et al. \(2010\)](#) in order to increase cell thickness in the layers nearest the ground, allowing longer timesteps. [Leuenberger et al. \(2010\)](#) found the exponent has an optimal value of  $n = 1.35$ . Choosing  $n = 1$  gives the decay functions used by [Schär et al. \(2002\)](#). While SLEVE can produce very smooth meshes, the coordinate transform becomes non-monotonic and the SLEVE mesh becomes tangled if parameter values are chosen poorly ([Schär et al., 2002; Leuenberger et al., 2010](#)), making it difficult to produce a very smooth global mesh with real terrain (C. Kühnlein 2015, personal communication). Many operational atmospheric models use some form of coordinate smoothing ([Eckermann, 2009](#)), and this approach has been found to reduce pressure gradient errors ([Schär et al., 2002; Leuenberger et al., 2010; Klemp, 2011](#)).

The second approach to reducing pressure gradient errors is to improve the accuracy in calculating the horizontal pressure gradient itself. Instead of calculating the horizontal pressure gradient in the computational domain, the techniques proposed by [Klemp \(2011\)](#) and [Zängl \(2012\)](#) both involve interpolation onto  $z$  levels in the physical domain. This gave them the flexibility to design more accurate horizontal pressure gradient discretizations using more appropriate stencils.

Cut cell meshes are less distorted than any smoothed terrain-following mesh, and some studies have shown examples where cut cells produce more accurate results when compared to terrain-following meshes. Spurious winds seen using terrain-following meshes are not present with cut cells, and errors do not increase with steeper terrain ([Good et al., 2014](#)). A comparison of terrain-following and cut cell meshes using real initial data by [Steppeler et al. \(2013\)](#) found that 5-day forecasts of precipitation and wind over Asia in January 1989 were more accurate in the cut-cell model, although this result was dependent on using an old version of a model. Although cut cell meshes are almost entirely undistorted, when explicit methods are used with cut cells, the small cell problem must be overcome in order to avoid severe time-step constraints.

We seek a new type of mesh that improves pressure gradient calculations compared to terrain-following methods, and avoids the severe time-step constraints associated with arbitrarily small cut cells. Section 3.1 describes the slanted cell method which is designed to satisfy these criteria. Section 3.2 presents a new two-dimensional test that challenges transport schemes by transporting a tracer along the ground through slanted cells, and this test is used to measure time-step constraints for terrain-following, cut cell and slanted cell meshes. Section 3.3 outlines the discretisation of the fully compressible model taken from [Weller and Shahrokhi \(2014\)](#) which includes a curl-free pressure gradient formulation. In section 3.4, the fully compressible model is used to simulate a standard resting atmosphere test case ([Klemp, 2011](#)), comparing results using terrain-following, cut cell and slanted cell meshes.

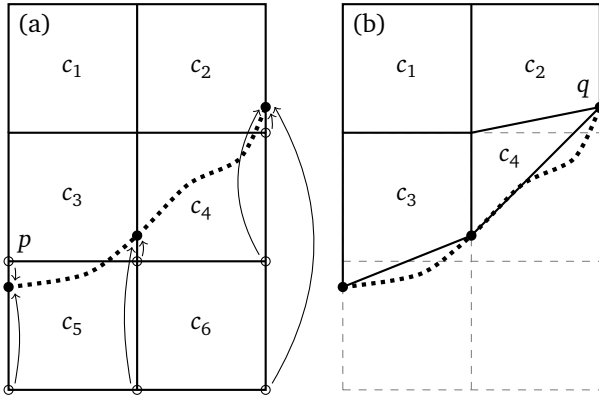


Figure 3.2: Illustration of a slanted cell mesh (a) before, and (b) after construction. The terrain surface, denoted by a heavy dotted line, intersects a uniform rectangular mesh comprising six cells,  $c_1, \dots, c_6$ . The cell vertices, marked by open circles, are moved to the points at which the terrain intersects vertical cell edges, marked by filled circles. Cells that have no volume are removed. Where a cell has two vertices occupying the same point, the zero-length edge that joins those vertices is removed. In this illustration, cells  $c_5$  and  $c_6$  are removed because they have no volume, and the zero-length edge at point  $q$  is removed to create a triangular cell,  $c_4$ . Point  $p$  is moved down because it is within  $2\Delta z/5$  of the surface, avoiding the creation of a thin cell.

### 3.1 Slanted cell method

The slanted cell method is straightforward, and slanted cell meshes are always free of mesh tangling by construction. Starting from a uniform rectangular mesh, all cell vertices that lie beneath the orography are moved up to the surface. Additionally, to avoid creating very thin cells, all vertices up to  $2\Delta z/5$  above the orography can be moved down to the surface. Where all four of a cell's vertices are moved, the cell has zero volume and so it is removed. Where two vertices at the same horizontal location are moved up to the surface they will occupy the same point; this results in a zero-length edge that is removed to create a triangular cell. Figure 3.2 shows how a  $2 \times 3$ -cell, uniform rectangular mesh is transformed into a slanted cell mesh. Cells  $c_5$  and  $c_6$  are removed because they have zero volume, and the zero-length edge at point  $q$  is removed to create a triangular cell,  $c_4$ . Point  $p$  is moved down because it is within  $2\Delta z/5$  of the surface, avoiding the creation of a very thin cell.

The slanted cell method does generate some small cells but, unlike the cut cell method, the width of slanted cells is never altered. Hence, slanted cell meshes should not suffer from severe time-step constraints associated with arbitrarily small cut cells. An example of a slanted cell mesh is illustrated in figure 3.1d for comparison with the equivalent BTF (figure 3.1a), SLEVE (figure 3.1b), and cut cell (figure 3.1c) meshes, with the same mesh spacing and mountain profile used for all meshes.

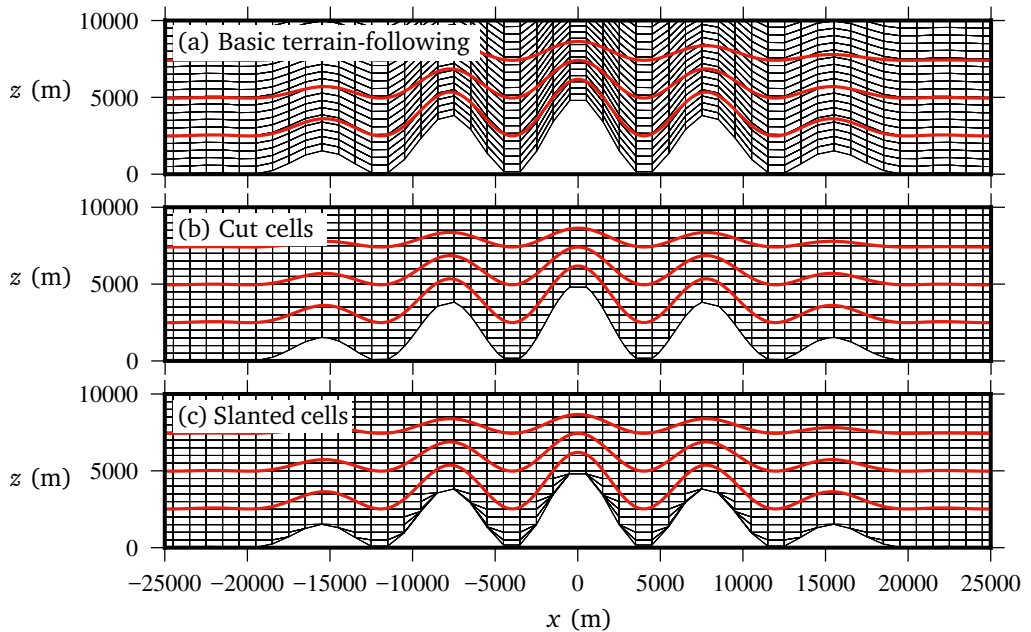


Figure 3.3: Two dimensional  $x$ - $z$  meshes created with the (a) basic terrain-following, (b) cut cell, and (c) slanted cell methods, used for the tracer transport tests in section 3.2. Cell edges are marked by thin black lines. The peak mountain height  $h_0 = 5$  km. The velocity field is the same for all mesh types with streamlines marked on each panel by thick red lines. The velocity field (equation 2.53) follows the lower boundary and becomes entirely horizontal above  $H_1 = 10$  km. Only the lowest 10 km for the central region of the domain is shown. The entire domain is 301 km wide and 25 km high.

### 3.2 Transport over a mountainous lower boundary

The two-dimensional tests performed in chapter 2 transported tracers positioned well above the terrain surface. Here we formulate a new test, positioning the tracer at the ground in order to assess the accuracy of transport schemes immediately above a mountainous lower boundary. Results using the cubicFit scheme are compared with the linearUpwind scheme on basic terrain-following, cut cell and slanted cell meshes. The test presents a particular challenge to transport schemes as they must transport the tracer through arbitrarily small cut cells and distorted slanted cells.

The domain size and mountain profile is the same as those in the horizontal tracer advection test in section 2.2, with a mesh spacing of  $\Delta x = 1000$  m and  $\Delta z = 500$  m. In order to present the most challenging test on slanted cell meshes, vertices are not moved downwards and so thin cells remain near mountain peaks. Cell edges in the central region of the domain are shown in figure 3.3 for each of the three mesh types. Cells in the BTF mesh are highly distorted over steep slopes (figure 3.3a) while the cut cell mesh (figure 3.3b) and slanted cell mesh (figure 3.3c) are orthogonal everywhere except for cells nearest the ground.

A velocity field is chosen that follows the terrain at the surface and becomes entirely horizontal

Mesh type	Peak mountain height $h_0$ (km)				
	0	3	4	5	6
BTF	40	16	10	8	5
Cut cell	40	1.6	1.6	0.5	1.6
Slanted cell	40	8	6.25	5	4

Table 3.1: Time-steps (s) for the two-dimensional transport test over a mountainous lower boundary. The time-steps were chosen so that the maximum Courant number was between 0.36 and 0.46.

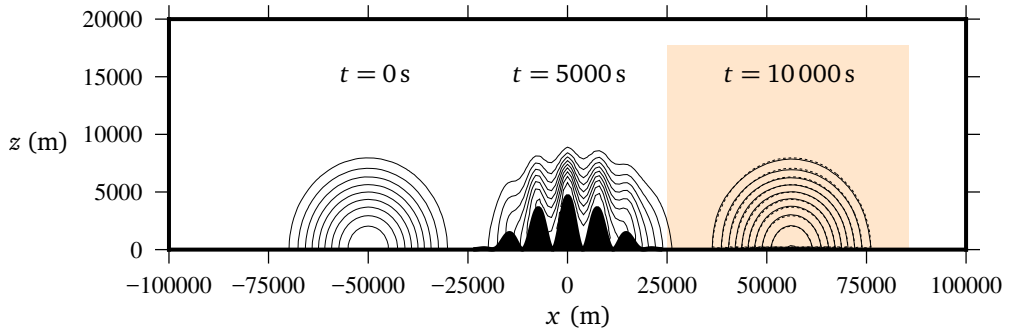


Figure 3.4: Evolution of the tracer in the two-dimensional transport test over a mountainous lower boundary. The tracer is transported to the right over the wave-shaped terrain. Tracer contours are every  $0.1 \text{ kg m}^{-3}$ . The result obtained using the cubicFit scheme on the basic terrain-following mesh is shown at  $t = 0 \text{ s}$ ,  $t = 5000 \text{ s}$  and  $t = 10 000 \text{ s}$  with solid black contours. The analytic solution at  $t = 10 000 \text{ s}$  is shown with dotted contours. The shaded box indicates the region that is plotted in figure 3.5.

above  $H_1 = 10 \text{ km}$ . The value of  $H_1$  is chosen to be much smaller than the domain height  $H$  in equation (2.47) so that flow crosses the surfaces of the BTF mesh. This is evident in figure 3.3a where the velocity streamlines are tangential to the mesh only at the ground. The flow is deliberately misaligned with the BTF, cut cell and slanted cell meshes away from the ground (figure 3.3) to ensure that flow always crosses mesh surfaces in order to challenge the transport schemes.

The tracer is defined again by equation (2.50) but is now positioned at the ground with  $(x_0, z_0) = (-50 \text{ km}, 0 \text{ km})$  with half-widths  $A_x = 25 \text{ km}$  and  $A_z = 10 \text{ km}$ . Tests are integrated forward for  $10 000 \text{ s}$ . The time-step was chosen for each mesh so that the maximum Courant number was about 0.4 (table 3.1). An analytic solution at  $10 000 \text{ s}$  is obtained by calculating the new horizontal position of the tracer using equation (2.58). By solving this equation we find that  $x(t = 10 000 \text{ s}) = 6244.087 \text{ m}$  when  $h_0 = 5 \text{ km}$ .

The tracer density boundary conditions are the same as those in section 2.2. Since the cubicFit transport scheme uses values at boundaries with Dirichlet boundary conditions, the cubicFit scheme uses only inlet boundary values in this test case.

Three series of tests were performed using similar configurations. The first series uses a peak

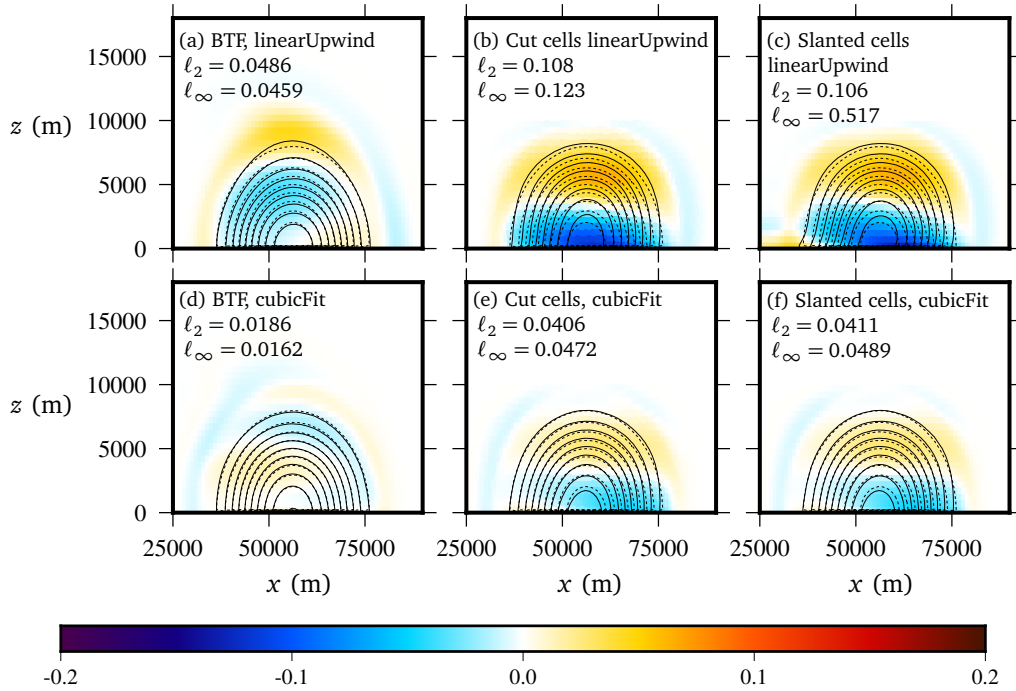


Figure 3.5: Tracer contours at  $t = 10\,000$  s for the two-dimensional tracer transport tests over a mountainous lower boundary. A region in the lee of the mountain is plotted corresponding to the shaded area in figure 3.4. Results are presented on BTF, cut cell and slanted cell meshes (shown in figure 3.3) using the linearUpwind and cubicFit transport schemes. The numerical solutions are marked by solid black lines. The analytic solution is marked by dotted lines. Contours are every  $0.1 \text{ kg m}^{-3}$ .

mountain height of  $h_0 = 5 \text{ km}$  to examine errors on different mesh types using the two transport schemes. The second series varies the peak mountain height to examine the sensitivity of the transport schemes to mesh distortions. The third series verifies accuracy at Courant numbers close to the limit of stability, and examines the longest stable time-step for different mesh types.

### A comparison of numerical accuracy between mesh types and transport schemes

For the first series of tests with  $h_0 = 5 \text{ km}$ , tracer contours at the initial time  $t = 0 \text{ s}$ , half-way time  $t = 5000 \text{ s}$ , and end time  $t = 10\,000 \text{ s}$  are shown in figure 3.4 using the cubicFit scheme on the BTF mesh. As apparent at  $t = 5000 \text{ s}$ , the tracer is distorted by the terrain-following velocity field as it passes over the mountain, but its original shape is restored once it has cleared the mountain by  $t = 10\,000 \text{ s}$ . Slight errors are apparent when the numerical solution marked with solid contour lines is compared with the analytic solution marked with dotted contour lines.

Numerical errors are more clearly revealed by subtracting the analytic solution from the numerical solution. Error fields are compared between BTF, cut cell and slanted cell meshes using the linearUpwind scheme (figures 3.5a, 3.5b and 3.5c respectively) and the cubicFit scheme

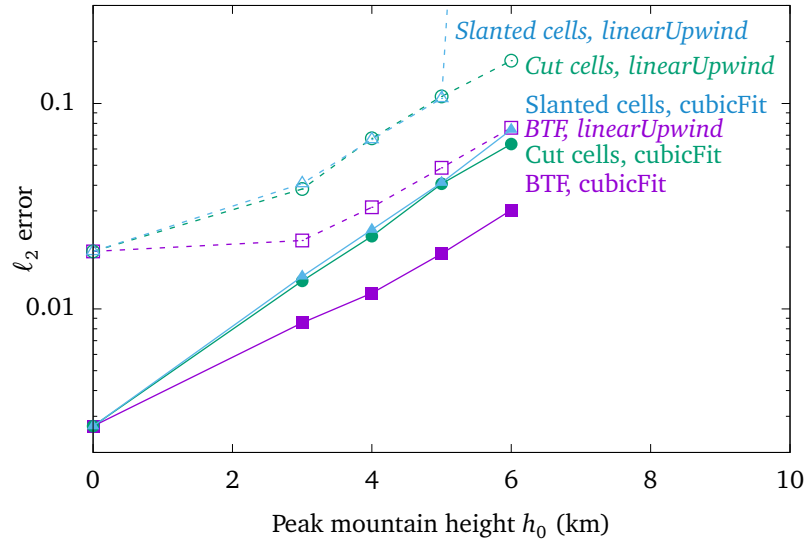


Figure 3.6: Error measures for the two-dimensional tracer transport tests over a mountainous lower boundary. Peak mountain heights  $h_0$  are from 0 km to 6 km. Results are compared on BTF, cut cell and slanted cell meshes using the linearUpwind and the cubicFit schemes. At  $h_0 = 0$  km the terrain is entirely flat and the BTF, cut cell and slanted cell meshes are identical. At  $h_0 = 6$  km the linearUpwind scheme is unstable on the slanted cell mesh.

(figures 3.5d, 3.5e and 3.5f respectively). Results are least accurate using the linearUpwind scheme on the slanted cell mesh (figure 3.5c) with the final tracer being slightly distorted. The  $\ell_\infty$  error magnitude is reduced by using the linearUpwind scheme on the cut cell mesh (figure 3.5b), but the shape of the error remains the same. On the BTF mesh (figure 3.5d), cut cell mesh (figure 3.5e) and slanted cell mesh (figure 3.5f), the cubicFit scheme is more accurate than the linearUpwind scheme.

### Numerical stability and numerical accuracy with increasingly steep slopes

To further examine the performance of the cubicFit scheme in the presence of steep terrain, a second series of tests were performed in which the peak mountain height was varied from 0 km to 6 km keeping all other parameters constant. Results were obtained on BTF, cut cell and slanted cell meshes using the linearUpwind scheme and cubicFit scheme. Again, the time-step was chosen for each test so that the maximum Courant number was about 0.4 (table 3.1). The  $\ell_2$  error was calculated by subtracting the analytic solution from the numerical solution (figure 3.6). Note that the analytic solution is a function of mountain height, with the tracer travelling farther over higher mountains due to non-divergent flow through a narrower channel. In all cases, error increases with increasing mountain height because steeper slopes lead to greater mesh distortions. Errors are identical for a given transport scheme when  $h_0 = 0$  km and the ground is entirely flat because the BTF, cut cell and slanted cell meshes are identical. The linearUpwind

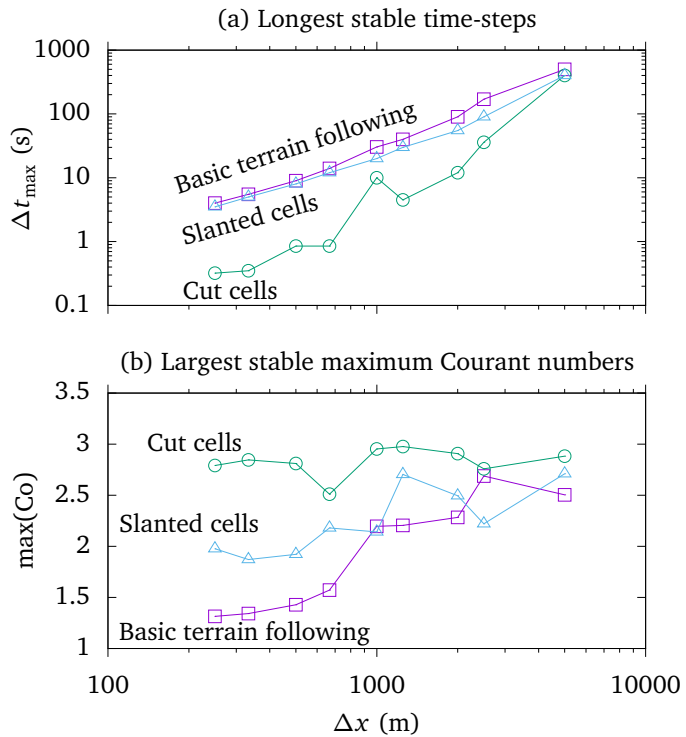


Figure 3.7: (a) Longest stable time-steps,  $\Delta t_{\max}$ , and (b) largest stable maximum Courant numbers,  $\max(Co)$ , for the two-dimensional tracer transport test over a mountainous lower boundary. Results were obtained on basic terrain-following, cut cell and slanted cell meshes at mesh spacings between  $\Delta x = 5000$  m and  $\Delta x = 250$  m. The largest stable maximum Courant numbers were calculated from the corresponding longest stable time-steps using equation (2.4).

scheme is unstable on the slanted cell mesh with a peak mountain height  $h_0 = 6$  km despite using a Courant number of 0.428. The cubicFit scheme yields stable results in all tests, and cubicFit is more accurate than linearUpwind in all tests.

### Numerical stability limits of the cubicFit transport scheme

A final series of tests were performed to determine the stability limit of the cubicFit scheme with the two-stage Heun time-stepping scheme (equation 2.2). The tracer was transported on BTF, slanted cell and cut cell meshes with a variety of mesh spacings between  $\Delta x = 5000$  m and  $\Delta x = 125$  m.  $\Delta z$  was chosen so that a constant aspect ratio is preserved such that  $\Delta x/\Delta z = 2$ . For each test, the time-step was increased until the result became unstable. The largest stable time-steps,  $\Delta t_{\max}$ , are presented in figure 3.7a. BTF meshes permit the longest time-steps of all three mesh types since cells are almost uniform in volume. As expected, the longest stable time-step scales linearly with BTF mesh spacing. There is no such linear scaling on cut cell meshes because these meshes can have arbitrarily small cells. The time-step constraints on cut cell meshes are the most severe of the three mesh types. Slanted cell meshes have a slightly

stronger time-step constraint than BTF meshes but still exhibit similar linear scaling with mesh spacing.

Figure 3.7b presents the largest stable maximum Courant numbers,  $\max(\text{Co})$ , which were calculated by substituting  $\Delta t = \Delta t_{\max}$  into equation (2.4). On basic terrain following meshes, the maximum Courant number tends towards about 1.3 with finer mesh spacings. No such trend is found on cut cell or slanted cell meshes. Cut cell meshes permit the largest maximum Courant numbers of around 3, but the largest stable time-steps on cut cell meshes are still smaller than corresponding time-steps on basic terrain following and slanted cell meshes.

This thesis focuses on the spatial discretisation of the cubicFit scheme, but the stability limit depends also upon the choice of time-stepping. We have not calculated a theoretical Courant number limit, although such an analysis should be possible using the techniques in (Baldauf, 2008).

This new test case demonstrates that the cubicFit transport scheme is more accurate than the linearUpwind scheme on all meshes, and only the cubicFit scheme can achieve stable results on slanted cell meshes with very steep slopes. The slanted cell method exhibits a time-step constraint that scales linearly with mesh spacing, and slanted cells avoid severe time-step constraints associated with arbitrarily small cut cells. Next, we incorporate the cubicFit transport scheme into a model of the fully compressible Euler equations.

### 3.3 Discretisation of the fully compressible Euler equations

The finite volume model of the fully compressible Euler equations is taken from Weller and Shahrokhi (2014), given by

$$\text{Momentum} \quad \frac{\partial \rho \mathbf{u}}{\partial t} + \nabla \cdot \rho \mathbf{u} \otimes \mathbf{u} = \rho \mathbf{g} - c_p \rho \theta \nabla \Pi - \mu \rho \mathbf{u} \quad (3.4a)$$

$$\text{Continuity} \quad \frac{\partial \rho}{\partial t} + \nabla \cdot \rho \mathbf{u} = 0 \quad (3.4b)$$

$$\text{Thermodynamic equation} \quad \frac{\partial \rho \theta}{\partial t} + \nabla \cdot \rho \mathbf{u} \theta = 0 \quad (3.4c)$$

$$\text{Ideal gas law} \quad \Pi^{(1-\kappa)/\kappa} = \frac{R \rho \theta}{p_0} \quad (3.4d)$$

where  $\rho$  is the density,  $\mathbf{u}$  is the velocity field,  $\mathbf{g}$  is the gravitational acceleration,  $c_p$  is the heat capacity at constant pressure,  $\theta = T(p_0/p)^\kappa$  is the potential temperature,  $T$  is the temperature,  $p$  is the pressure,  $p_0 = 1000 \text{ hPa}$  is a reference pressure,  $\Pi = (p/p_0)^\kappa$  is the Exner function of pressure, and  $\kappa = R/c_p$  is the gas constant to heat capacity ratio.  $\mu$  is a damping function that can be used to absorb momentum near the upper boundary.

The model uses the C-grid staggering in the horizontal and the Lorenz staggering in the vertical such that  $\theta$ ,  $\rho$  and  $\Pi$  are stored at cell centroids and the covariant component of velocity at cell faces. The model is configured without Coriolis forces.

Acoustic and gravity waves are treated implicitly and transport terms are treated explicitly. The trapezoidal implicit treatment of fast waves and the Hodge operator suitable for non-orthogonal meshes are described in the appendix to [Shaw and Weller \(2016\)](#). To avoid time-splitting errors between transport and fast waves, transport is time-stepped using a three-stage, second-order Runge-Kutta scheme. The transport terms of the momentum equation (3.4a) and thermodynamic equation (3.4c) are discretised in flux form using the cubicFit transport scheme.

This model is suitable for arbitrary meshes and includes a curl-free pressure gradient formulation. In the next section, we use this model to compare the accuracy of pressure gradient calculations using terrain-following, cut cell and slanted cell meshes.

### 3.4 Stratified atmosphere initially at rest

Diurnal valley and slope flows are associated with weak synoptic-scale winds, and cold air that sinks along sloping terrain can stagnate for days after becoming trapped in topographic basins ([Chow et al., 2013](#)). The test case by [Klemp \(2011\)](#) is an idealised representation of such phenomena, in which a wave-shaped mountain is submerged in a stably stratified atmosphere at rest in hydrostatic balance. The analytic solution is time-invariant, but numerical errors in calculating pressure gradients can give rise to spurious flows which become stronger over steeper terrain ([Klemp, 2011](#)). Results are compared using terrain-following, cut cell and slanted cell meshes.

Following [Klemp \(2011\)](#), the domain is 200 km wide and 20 km high, and the mesh spacing is  $\Delta x = \Delta z^* = 500$  m. All boundary conditions are no normal flow. The wave-shaped mountain profile has a surface height,  $h$ , given by

$$h(x) = h_0 \exp\left(-\left(\frac{x}{a}\right)^2\right) \cos^2(\alpha x) \quad (3.5)$$

where  $a = 5$  km is the mountain half-width  $\lambda = 4$  km is the wavelength and  $h_0$  is the peak mountain height. For the optimised SLEVE mesh, the coarse-scale component  $h_1$  is specified as

$$h_1(x) = \frac{1}{2}h_0 \exp\left(-\left(\frac{x}{a}\right)^2\right). \quad (3.6)$$

To accommodate a range of mountain heights we choose a coarse scale height  $s_1 = 20$  km and a fine scale height  $s_2 = 8$  km. Following [Leuenberger et al. \(2010\)](#) the optimal exponent value of  $n = 1.35$  is used. These parameter values result in a SLEVE mesh that is more distorted than the SLEVE mesh used by [Klemp \(2011\)](#), but the choice is necessary to avoid mesh tangling with mountains higher than 1 km.

The initial potential temperature field has  $\theta(z = 0) = 288$  K and a constant static stability with Brunt-Väisälä frequency  $N = 0.01$  s $^{-1}$  everywhere, except for a more stable layer of  $N = 0.02$  s $^{-1}$  between  $2$  km  $\leq z \leq 3$  km. The Exner function of pressure is calculated so that it is in discrete hydrostatic balance in the vertical direction ([Weller and Shahrokhi, 2014](#)). The damping function  $\mu$  is set to 0 s $^{-1}$ . Unlike [Klemp \(2011\)](#), there is no eddy diffusion in the equation set.

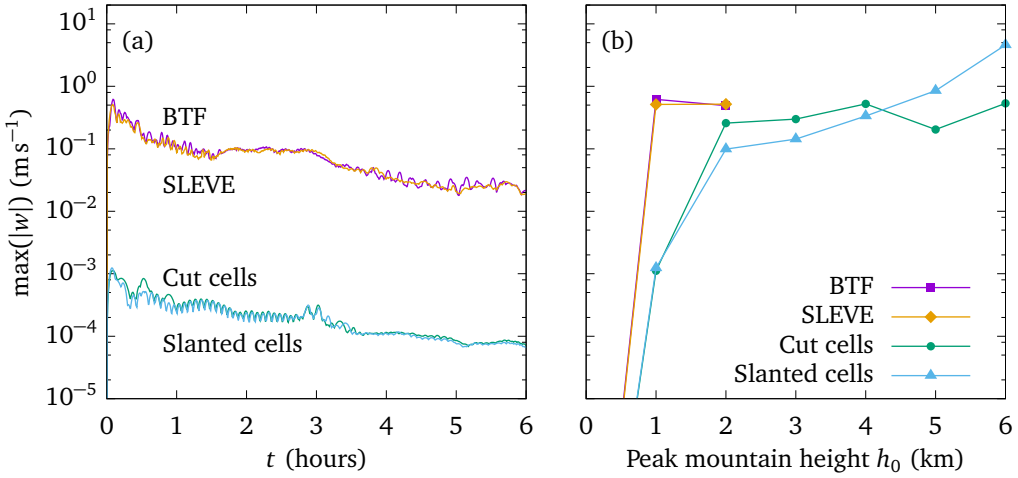


Figure 3.8: Spurious vertical velocities in the resting atmosphere test using BTF, SLEVE, cut cell and slanted cell meshes. (a) Time series of spurious vertical velocities, with the maximum absolute value calculated at each time-step. (b) Sensitivity to peak mountain height  $h_0$ , with the maximum absolute value calculated across all time-steps.

The test is integrated forward by 6 hours using a time-step of  $\Delta t = 25$  s on the BTF, SLEVE, cut cell and slanted cell meshes with a peak mountain height  $h_0 = 1$  km. For each mesh, the maximum absolute vertical velocity is calculated at each time-step as a measure of the spurious flow generated by numerical pressure gradient errors. In agreement with (Klemp, 2011), magnitudes of vertical velocity peak shortly after integration begins and magnitudes are larger on more distorted meshes (figure 3.8a). However, magnitudes are much smaller comparing results on the terrain-following meshes with those from Klemp (2011): results in figure 3.8a, which use a curl-free pressure gradient formulation, have maximum absolute vertical velocities of  $0.62 \text{ m s}^{-1}$ , compared with a maximum of  $\sim 7 \text{ m s}^{-1}$  found by Klemp (2011) using their improved horizontal pressure gradient formulation. The results on terrain-following meshes in figure 3.8a have similar maximum errors as Weller and Shahrokh (2014) but, due to the more stable split into implicitly and explicitly treated terms (described in the appendix to Shaw and Weller (2016)), the errors decay over time due to the *TODO: dissipative? what exactly is meant by dissipative?* nature of the transport scheme. Unlike the result from Klemp (2011), spurious flows are similar on both terrain-following meshes even though the SLEVE mesh is less distorted than the BTF mesh.

Compared to results on the terrain-following meshes, spurious flows are two orders of magnitude smaller on the cut cell mesh and the slanted cell mesh with a maximum absolute vertical velocity of  $\sim 1 \times 10^{-3} \text{ m s}^{-1}$ . Good et al. (2014) found the maximum vertical velocity in their cut cell model was  $1 \times 10^{-12} \text{ m s}^{-1}$ , which is better than any result obtained here. It is worth noting that our model stores values at the geometric centre of cut cells, whereas the model used by Good et al. (2014) has cell centres at the centre of the uncut cell, resulting in the centre of

some cut cells being below the ground (S.-J. Lock 2014, personal communication). This means that the mesh is effectively regular when calculating horizontal and vertical gradients, and this would account for the very small velocities found by [Good et al. \(2014\)](#).

To evaluate the slanted cell method with steeper slopes, we perform a second series of tests with peak mountain heights ranging from  $h_0 = 0\text{ km}$  to  $h_0 = 6\text{ km}$ . The BTF, SLEVE, cut cell and slanted cell meshes with the largest peak mountain height of  $h_0 = 6\text{ km}$  are shown in figure 3.1. To obtain a single measure of spurious flow for a given mesh, the maximum absolute vertical velocity is calculated across all time-steps. The most accurate results are obtained without mountains when  $h_0 = 0\text{ km}$  when all meshes become identical, with  $\max(|w|) \sim 1 \times 10^{-11}\text{ m s}^{-1}$ . Using terrain-following meshes, the model becomes unstable beyond  $h_0 = 2\text{ km}$ . Using cut cell meshes, maximum vertical velocities are almost constant at  $\sim 0.5\text{ m s}^{-1}$  beyond  $h_0 = 1\text{ km}$  because cut cell mesh distortions are largely independent of mountain height. Using slanted cell meshes, maximum vertical velocities are one to two orders of magnitude smaller than those found on terrain-following meshes at a given mountain height. Unlike results on terrain-following meshes, slanted cell meshes yield stable results for all mountain heights, although maximum vertical velocities increase with peak mountain height as slanted cells become increasingly distorted. Up to a peak mountain height of  $h_0 = 4\text{ km}$ , slanted cell meshes produce results that are more accurate than those obtained for any other mesh.

In summary, spurious velocities in the resting atmosphere test were similar on both terrain-following meshes, with errors being much smaller compared to those from [Klemp \(2011\)](#). The maximum absolute vertical velocity was decreased by one to two orders of magnitude using cut cell and slanted cell meshes, so we conclude that, in this test, mesh distortion, or lack of alignment of the mesh with surfaces of constant gravitational potential, are the primary cause of numerical error. The resting atmosphere test presented a challenge to the pressure gradient formulation but the resultant spurious flows presented no particular challenge to the cubicFit transport scheme. We will turn our attention to transport-dominated flow in the next chapter.

## 4 Generalising the Charney–Phillips staggering for arbitrary meshes

---

### 4.1 Schär mountain waves

TODO:

- *Meshes: BTF cut cell, slanted cell, SLEVE?*
- *Conclusion: linearUpwind is insufficiently accurate on the BTF mesh*
- *Conclusion: unlike linearUpwind, cubicFit gives the correct solution on the BTF mesh*
- *Conclusion: linearUpwind BTF solution similar to non-cancellation of metric terms in (Klemp et al., 2003)*
- *Conclusion: cubicFit produces almost identical results on BTF cut cell and slanted cell meshes. Unlike the results in (Shaw and Weller, 2016), errors in potential temperature are negligible using the cubicFit scheme.*
- *Conclusion: should we test max(dt) again? we've not yet done so for a dynamical test. I'd hope that slanted cells are much better than cut cells.*

TODO: *Charney–Phillips aspects:*

- *mesh: BTF, BTF + edgeGrading on vertical faces?*
- *conclusion: CP formulation works for advection-dominated flow, but advection scheme is not sufficiently accurate to obtain the correct solution (this is not surprising since advectiveFoamF is less accurate than advectionFoam with linearUpwind, and we already know that ExnerFoamH+linearUpwind is also inaccurate for schaerWaves test)*
- *conclusion: flow over mountains can also excite the Lorenz computational mode but less clearly than our more artificial test case?*

- *conclusion: ExnerFoamCP again eliminates computational mode?*

The test originally specified by Schär et al. (2002) prescribes flow over terrain with small-scale and large-scale undulations which induces propagating and evanescent gravity waves. **TODO:** what is the motivation for this test? it is needed to assess the dynamics solver with horizontal and vertical transport

Following Melvin et al. (2010), the domain is 300 km wide and 30 km high, and the mesh spacing is  $\Delta x = 500$  m and  $\Delta z^* = 300$  m. The mountain profile has the same form as equation (3.5), but the mountain waves test has a lower peak mountain height of  $h_0 = 250$  m. As in the resting atmosphere test,  $a = 5$  km is the mountain half-width and  $\lambda = 4$  km is the wavelength.

A uniform horizontal wind  $(u, w) = (10, 0)$  m s<sup>-1</sup> is prescribed in the interior domain and at the inlet boundary. No normal flow is imposed at the top and bottom boundaries and the velocity field has a zero gradient outlet boundary condition.

The initial thermodynamic conditions have constant static stability with  $N = 0.01$  s<sup>-1</sup> everywhere such that

$$\theta(z) = \theta_0 \exp\left(\frac{N^2}{g}z\right) \quad (4.1)$$

where the temperature at  $z = 0$  is  $\theta_0 = 288$  K. Potential temperature values are prescribed at the inlet and upper boundary using equation (4.1), and a zero gradient boundary condition is applied at the outlet. At the ground, fixed gradients are imposed by calculating the component of  $\nabla\theta$  normal to each face using the vertical derivative of equation (4.1). For the Exner function of pressure, hydrostatic balance is prescribed on top and bottom boundaries and the inlet and outlet are zero normal gradient.

Sponge layers are added to the upper 10 km and leftmost 10 km at the inlet boundary to damp the reflection of waves. The damping function,  $\mu$ , is adapted from Melvin et al. (2010) such that

$$\mu(x, z) = \mu_{\text{upper}} + \mu_{\text{inlet}} \quad (4.2)$$

$$\mu_{\text{upper}}(z) = \begin{cases} \bar{\mu} \sin^2\left(\frac{\pi}{2} \frac{z-z_B}{H-z_B}\right) & \text{if } z \geq z_B \\ 0 & \text{otherwise} \end{cases} \quad (4.3)$$

$$\mu_{\text{inlet}}(x) = \begin{cases} \bar{\mu} \sin^2\left(\frac{\pi}{2} \frac{x_I-x}{x_I-x_0}\right) & \text{if } x < x_I \\ 0 & \text{otherwise} \end{cases} \quad (4.4)$$

where  $\bar{\mu} = 1.2$  s<sup>-1</sup> is the damping coefficient,  $z_B = 20$  km is the bottom of the sponge layer,  $H = 30$  km is the top of the domain,  $x_0 = -150$  km is the leftmost limit of the domain and  $x_I = -140$  km is the rightmost extent of the inlet sponge layer. The sponge layer is only active on faces whose normal is vertical so that it damps vertical momentum only. Note that, while the domain itself is 30 km in height, for the purposes of generating BTF meshes, the domain height is set to 20 km because the sponge layer occupies the uppermost 10 km.

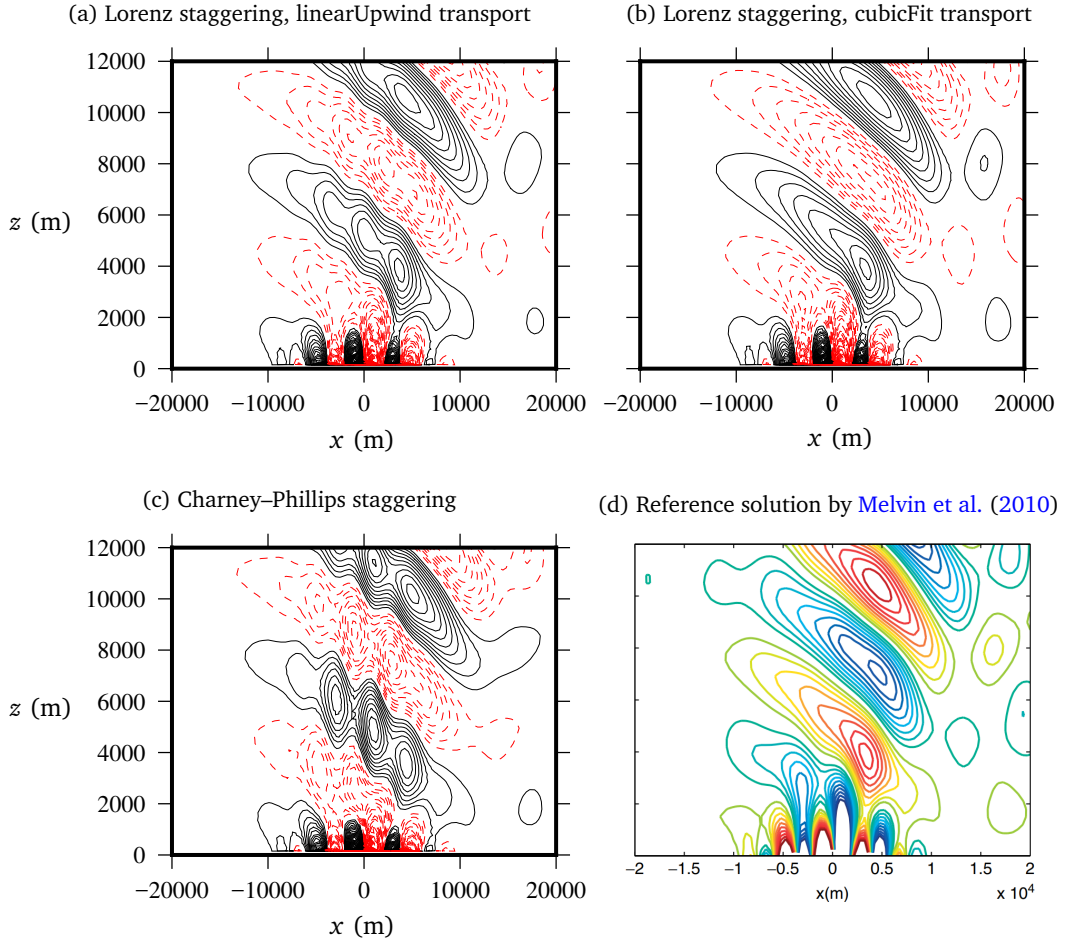
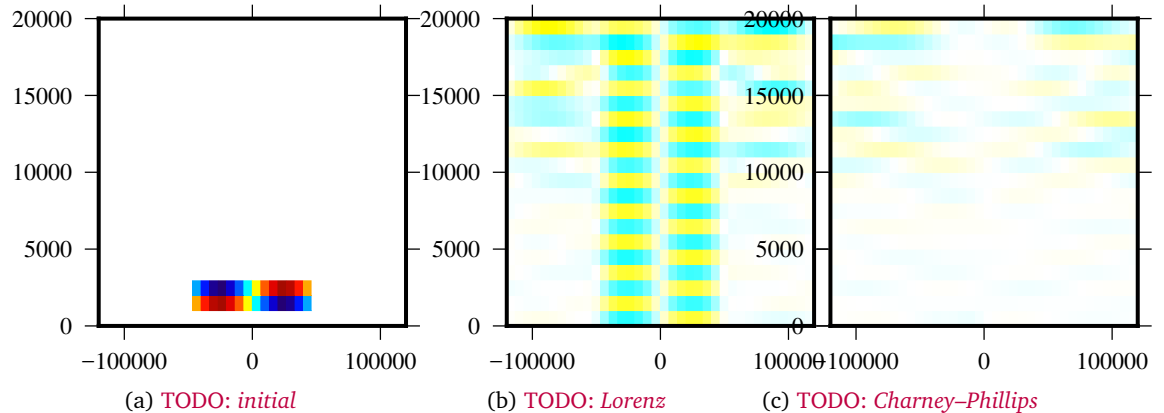


Figure 4.1: Vertical velocities at the end of integration of the Schär mountain waves test case. Results obtained using a BTF mesh and Lorenz staggering, with potential temperature and momentum transported by (a) the linearUpwind scheme and (b) the cubicFit scheme, and (c) using a BTF mesh and Charney-Phillips staggering. For comparison, (d) provides a reference solution obtained with a mass-conserving semi-implicit semi-Lagrangian model (Melvin et al., 2010). Contours are plotted every  $0.05 \text{ m s}^{-1}$ . In figures (a), (b) and (c), ascending velocities are marked by solid black lines and descending velocities are marked by dashed red lines.

Figure 4.2: TODO: *theta\_diffs*

## 4.2 Advective-form transport for arbitrary Charney–Phillips meshes

TODO: describe the CP advection scheme: `interpGrad+fvcReconstructCP` (advective form)

## 4.3 A new test case to excite the Lorenz computational mode

TODO:

- Test: 2D vertical slice with initial  $\theta$  perturbation, `ExnerFoamH` and `ExnerFoamCP`
- Meshes: uniform, edgeGrading (sloping horizontal surfaces, sloping vertical faces)
- Plot: horizontal edgeGrading, vertical edgeGrading
- Plot: initial  $\theta_{\text{diff}}$ , final  $\theta_{\text{diff}}$  for `ExnerFoamH` and `ExnerFoamCP`
- Plot: conservation of internal energy and total energy time series, `ExnerFoamH` and `ExnerFoamCP`, uniform mesh, horizontal edgeGrading, vertical edgeGrading
- Conclusion: the test excites the Lorenz computational mode with `ExnerFoamH`
- Conclusion: `ExnerFoamCP` eliminates computational mode
- Conclusion: edgeGrading reveals lack of conservation... is it due to the advective form transport of  $\theta$ ? next test will try to provide an answer

## 4.4 Horizontal transport on distorted Charney–Phillips meshes

TODO:

- *Test: horizontal advection; advectiveFoamF, advectionFoam with linear interp, advectionFoam with linearUpwind interp; measure l2 and linf errors (s.t. they can be compared with cell-centred, C-grid results); uniform and edgeGraded meshes*
- *Plot: error fields, analytic+numerical contours of final solution, which schemes and which meshes? too many combinations to plot all of them*
- *Plot: time-series of conservation, ExnerFoamH and ExnerFoamCP, uniform mesh, horizontal edgeGrading, vertical edgeGrading*
- *Conclusion: advection is conservative on uniform meshes, non-conservative on non-uniform meshes*
- *Conclusion: advectiveFoamF errors are comparable to advectionFoam with linear interpolation?*
- *Conclusion: advectiveFoamF errors are worse than advectionFoam with linearUpwind interpolation?*

## 5 Conclusion

---

## **Appendices**

## A Mesh geometry on a spherical Earth

---

The cubicFit transport scheme is implemented using the OpenFOAM CFD library. Unlike many atmospheric models that use spherical coordinates, OpenFOAM uses global, three-dimensional Cartesian coordinates with the  $z$ -axis pointing up through the North pole. In order to perform the experiments on a spherical Earth presented in section 2.4, it is necessary for velocity fields and mesh geometries to be expressed in these global Cartesian coordinates.

### Velocity field specification

The non-divergent velocity field in section 2.4 is specified as a streamfunction  $\Psi(\lambda, \theta)$ . Instead of calculating velocity vectors, the flux  $\mathbf{u}_f \cdot \mathbf{s}_f$  through a face  $f$  is calculated directly from the streamfunction,

$$\mathbf{u}_f \cdot \mathbf{s}_f = \sum_{e \in f} \mathbf{e} \cdot \mathbf{x}_e \Psi(e) \quad (\text{A.1})$$

where  $e \in f$  denotes the edges  $e$  of face  $f$ ,  $\mathbf{e}$  is the edge vector joining the two vertices of the edge,  $\mathbf{x}_e$  is the position vector of the edge midpoint, and  $\Psi(e)$  is the streamfunction evaluated at the same position. Edge vectors are directed in a counter-clockwise orientation.

### Spherical mesh construction

Since OpenFOAM does not support two-dimensional spherical meshes, instead, we construct meshes that have a single layer of cells that are 2000 m deep, having an inner radius  $r_1 = R_e - 1000$  m and an outer radius  $r_2 = R_e + 1000$  m. By default, OpenFOAM meshes comprise polyhedral cells with straight edges and flat faces. This is problematic for spherical meshes because face areas and cell volumes are too small. For tests on a spherical Earth, we override the default configuration and calculate our own face areas, cell volumes, face centres and cell centres that account for the mesh curvature. Note that the new centres are no longer centroids, but they are consistent with the horizontal transport tests on a sphere presented in section 2.4.

A face is classified as either a surface face or radial face. A surface face has any number of vertices, all of equal radius. A radial face has four vertices with two different radii,  $r_1$  and  $r_2$ ,

and two different horizontal coordinates,  $(\lambda_1, \theta_1)$  and  $(\lambda_2, \theta_2)$ . A radial face centre is modified so that it has a radius  $R_e$ . The latitudinal and longitudinal components of a radial face centre need no modification. The face area  $A_f$  for a radial face  $f$  is the area of the annular sector,

$$A_f = \frac{d}{2} |r_2^2 - r_1^2| \quad (\text{A.2})$$

where  $d$  is the great-circle distance between  $(\lambda_1, \theta_1)$  and  $(\lambda_2, \theta_2)$ .

To calculate the centre of a surface face  $f$ , a new vertex is created that is positioned at the mean of the face vertices. Note that this centre position,  $\tilde{\mathbf{c}}_f$ , is used in intermediate calculations and it is not the face centre position. Next, the surface face is subdivided into spherical triangles that share this new vertex (Van Brummelen, 2013). The face centre direction and radius are calculated separately. The face centre direction  $\hat{\mathbf{r}}$  is the mean of the spherical triangle centres weighted by their solid angle,

$$\hat{\mathbf{r}} = \frac{\sum_{t \in f} \Omega_t (\mathbf{x}_{t,1} + \mathbf{x}_{t,2} + \tilde{\mathbf{c}}_f)}{|\sum_{t \in f} \Omega_t (\mathbf{x}_{t,1} + \mathbf{x}_{t,2} + \tilde{\mathbf{c}}_f)|} \quad (\text{A.3})$$

where  $t \in f$  denotes the spherical triangles  $t$  of face  $f$ ,  $\Omega_t$  is spherical triangle's solid angle which is calculated using l'Huilier's theorem,  $\mathbf{x}_{t,1}$  and  $\mathbf{x}_{t,2}$  are the positions of the vertices shared by the face  $f$  and spherical triangle  $t$ , and  $\tilde{\mathbf{c}}_f$  is the position of the centre vertex shared by all spherical triangles of face  $f$ . The face centre radius  $r$  is the mean radius of the face vertices, again weighted by the solid angle of each spherical triangle,

$$r = \frac{\sum_{t \in f} \Omega_t (|\mathbf{x}_{t,1}| + |\mathbf{x}_{t,2}|) / 2}{\Omega_f} \quad (\text{A.4})$$

where the solid angle  $\Omega_f$  of face  $f$  is the sum of the solid angles of the constituent spherical triangles,

$$\Omega_f = \sum_{t \in f} \Omega_t . \quad (\text{A.5})$$

We use equations (A.3) and (A.4) to calculate the centre  $\mathbf{c}_f$  of the face  $f$ ,

$$\mathbf{c}_f = r \hat{\mathbf{r}} \quad (\text{A.6})$$

The area vector  $\mathbf{S}_f$  of the surface face  $f$  is the sum of the spherical triangle areas (Van Brummelen, 2013),

$$\mathbf{S}_f = r^2 \Omega_f \hat{\mathbf{r}} . \quad (\text{A.7})$$

Cell centres and cell volumes are corrected by considering faces that are not normal to the sphere such that

$$\frac{(\mathbf{S}_f \cdot \mathbf{c}_f)^2}{|\mathbf{S}_f|^2 |\mathbf{c}_f|^2} > 0 . \quad (\text{A.8})$$

Let  $\mathcal{F}$  be the set of faces satisfying equation (A.8). Then, the cell volume  $\mathcal{V}_c$  is

$$\mathcal{V}_c = \frac{1}{3} \sum_{f \in \mathcal{F}} \mathbf{s}_f \cdot \mathbf{c}_f \quad (\text{A.9})$$

which can be thought of as the area  $A$  integrated between  $r_1$  and  $r_2$  such that  $\int_0^R A(r) dr = \int_{r_1}^{r_2} r^2 \Omega dr = \frac{1}{3} \Omega (r_2^3 - r_1^3)$ . The cell centre is modified so that it has a radius  $R_e$ , which is consistent with radial faces.

Edges can be classified in a similar manner to faces where surface edges are tangent to the sphere and radial faces are normal to the sphere. The edge midpoints  $\mathbf{x}_e$  are used to calculate the face flux for non-divergent velocity fields (equation A.1). For transport tests, corrections to edge midpoints are unnecessary. Due to the choice of  $r_1$  and  $r_2$  during mesh construction, the midpoint of a radial edge is at a radial distance of  $R_e$  which is necessary for the correct calculation of non-divergent velocity fields. The position of surface edge midpoints is unimportant because these edges do not contribute to the face flux since  $\mathbf{e} \cdot \mathbf{x}_e = 0$ . Edge lengths are the straight-line distance between the two vertices and not the great-circle distance. Again, the edge lengths are not corrected because it makes no difference to the face flux calculation.

## Bibliography

---

- Baldauf, M., 2008: Stability analysis for linear discretisations of the advection equation with Runge–Kutta time integration. *J. Comp. Phys.*, **227** (13), 6638–6659, doi:[10.1016/j.jcp.2008.03.025](https://doi.org/10.1016/j.jcp.2008.03.025).
- Cauquoin, A., and C. Risi, 2017: Importance of the advection scheme for the simulation of water isotopes over Antarctica by general circulation models: a case study with LMDZ-iso (LMDZ5a revision 1750). *Geosci. Model Dev.*, doi:[10.5194/gmd-2017-178](https://doi.org/10.5194/gmd-2017-178).
- CFD Direct, 2016: OpenFOAM user guide: Numerical schemes. <http://cfd.direct/openfoam/user-guide/fvschemes/>.
- Chen, Y., H. Weller, S. Pring, and J. Shaw, 2017: Comparison of dimensionally-split and multi-dimensional atmospheric transport schemes for long time-steps. *Quart. J. Roy. Meteor. Soc.*, doi:[10.1002/qj.3125](https://doi.org/10.1002/qj.3125).
- Chow, F. K., S. F. De Wekker, and B. J. Snyder, 2013: *Mountain weather research and forecasting: recent progress and current challenges*. Springer, doi:[10.1007/978-94-007-4098-3](https://doi.org/10.1007/978-94-007-4098-3).
- Cueto-Felgueroso, L., I. Colominas, J. Fe, F. Navarrina, and M. Casteleiro, 2006: High-order finite volume schemes on unstructured grids using moving least-squares reconstruction. Application to shallow water dynamics. *Int. J. Numer. Meth. Engng*, **65** (3), 295–331, doi:[10.1002/nme.1442](https://doi.org/10.1002/nme.1442).
- Cueto-Felgueroso, L., I. Colominas, X. Nogueira, F. Navarrina, and M. Casteleiro, 2007: Finite volume solvers and moving least-squares approximations for the compressible Navier–Stokes equations on unstructured grids. *196* (45), 4712–4736, doi:[10.1016/j.cma.2007.06.003](https://doi.org/10.1016/j.cma.2007.06.003).
- Durran, D. R., 2013: *Numerical methods for wave equations in geophysical fluid dynamics*, Vol. 32. Springer Science & Business Media, doi:[10.1007/978-1-4419-6412-0](https://doi.org/10.1007/978-1-4419-6412-0).
- Eckermann, S., 2009: Hybrid  $\sigma$ – $p$  coordinate choices for a global model. *Mon. Wea. Rev.*, **137** (1), 224–245, doi:[10.1175/2008MWR2537.1](https://doi.org/10.1175/2008MWR2537.1).

- Fast, J. D., 2003: Forecasts of valley circulations using the terrain-following and step-mountain vertical coordinates in the Meso-Eta model. *Wea. Forecasting*, **18**, 1192–1206, doi:[10.1175/1520-0434\(2003\)018<1192:FOVCUT>2.0.CO;2](https://doi.org/10.1175/1520-0434(2003)018<1192:FOVCUT>2.0.CO;2).
- Gal-Chen, T., and R. C. Somerville, 1975: On the use of a coordinate transformation for the solution of the Navier-Stokes equations. *J. Comp. Phys.*, **17** (2), 209–228, doi:[10.1016/0021-9991\(75\)90037-6](https://doi.org/10.1016/0021-9991(75)90037-6).
- Good, B., A. Gadian, S.-J. Lock, and A. Ross, 2014: Performance of the cut-cell method of representing orography in idealized simulations. *Atmos. Sci. Lett.*, **15** (1), 44–49, doi:[10.1002/asl2.465](https://doi.org/10.1002/asl2.465).
- Guo, W., R. D. Nair, and J.-M. Qiu, 2014: A conservative semi-Lagrangian discontinuous Galerkin scheme on the cubed sphere. *Mon. Wea. Rev.*, **142** (1), 457–475, doi:[10.1175/MWR-D-13-00048.1](https://doi.org/10.1175/MWR-D-13-00048.1).
- Heikes, R., and D. A. Randall, 1995a: Numerical integration of the shallow-water equations on a twisted icosahedral grid. Part I: Basic design and results of tests. *Mon. Wea. Rev.*, **123** (6), 1862–1880, doi:[10.1175/1520-0493\(1995\)123<1862:NIOTSW>2.0.CO;2](https://doi.org/10.1175/1520-0493(1995)123<1862:NIOTSW>2.0.CO;2).
- Heikes, R., and D. A. Randall, 1995b: Numerical integration of the shallow-water equations on a twisted icosahedral grid. Part II: A detailed description of the grid and an analysis of numerical accuracy. *Mon. Wea. Rev.*, **123** (6), 1881–1887, doi:[10.1175/1520-0493\(1995\)123<1881:NIOTSW>2.0.CO;2](https://doi.org/10.1175/1520-0493(1995)123<1881:NIOTSW>2.0.CO;2).
- Hoinka, K. P., and G. Zängl, 2004: The influence of the vertical coordinate on simulations of a PV streamer crossing the Alps. *Mon. Wea. Rev.*, **132** (7), 1860–1867, doi:[10.1175/1520-0493\(2004\)132<1860:TIOTVC>2.0.CO;2](https://doi.org/10.1175/1520-0493(2004)132<1860:TIOTVC>2.0.CO;2).
- Ii, S., and F. Xiao, 2009: High order multi-moment constrained finite volume method. Part I: Basic formulation. *J. Comp. Phys.*, **228** (10), 3669–3707, doi:[10.1016/j.jcp.2009.02.009](https://doi.org/10.1016/j.jcp.2009.02.009).
- Iske, A., and M. Käser, 2004: Conservative semi-Lagrangian advection on adaptive unstructured meshes. *Numer. Methods. Partial Differ. Equ.*, **20** (3), 388–411, doi:[10.1002/num.10100](https://doi.org/10.1002/num.10100).
- Kent, J., P. A. Ullrich, and C. Jablonowski, 2014: Dynamical core model intercomparison project: Tracer transport test cases. *Quart. J. Roy. Meteor. Soc.*, **140** (681), 1279–1293, doi:[10.1002/qj.2208](https://doi.org/10.1002/qj.2208).
- Klemp, J. B., 2011: A terrain-following coordinate with smoothed coordinate surfaces. *Mon. Wea. Rev.*, **139** (7), 2163–2169, doi:[10.1175/MWR-D-10-05046.1](https://doi.org/10.1175/MWR-D-10-05046.1).
- Klemp, J. B., W. C. Skamarock, and O. Fuhrer, 2003: Numerical consistency of metric terms in terrain-following coordinates. *Mon. Wea. Rev.*, **131** (7), 1229–1239, doi:[10.1175/1520-0493\(2003\)131<1229:NCOMTI>2.0.CO;2](https://doi.org/10.1175/1520-0493(2003)131<1229:NCOMTI>2.0.CO;2).

- Kühnlein, C., and P. K. Smolarkiewicz, 2017: An unstructured-mesh finite-volume MPDATA for compressible atmospheric dynamics. *J. Comp. Phys.*, **334**, 16–30, doi:[10.1016/j.jcp.2016.12.054](https://doi.org/10.1016/j.jcp.2016.12.054).
- Lashley, R. K., 2002: Automatic generation of accurate advection schemes on unstructured grids and their application to meteorological problems. Ph.D. thesis, University of Reading, 223 pp.
- Lauritzen, P., and Coauthors, 2014: A standard test case suite for two-dimensional linear transport on the sphere: results from a collection of state-of-the-art schemes. *Geosci. Model Dev.*, **7** (1), 105–145, doi:[10.5194/gmd-7-105-2014](https://doi.org/10.5194/gmd-7-105-2014).
- Lauritzen, P. H., C. Erath, and R. Mittal, 2011a: On simplifying ‘incremental remap’-based transport schemes. *J. Comp. Phys.*, **230** (22), 7957–7963, doi:[10.1016/j.jcp.2011.06.030](https://doi.org/10.1016/j.jcp.2011.06.030).
- Lauritzen, P. H., C. Jablonowski, M. A. Taylor, and R. D. Nair, 2011b: *Numerical techniques for global atmospheric models*, Vol. 80. Springer Science & Business Media, doi:[10.1007/978-3-642-11640-7](https://doi.org/10.1007/978-3-642-11640-7).
- Lauritzen, P. H., R. D. Nair, and P. A. Ullrich, 2010: A conservative semi-Lagrangian multi-tracer transport scheme (CSLAM) on the cubed-sphere grid. *J. Comp. Phys.*, **229** (5), 1401–1424, doi:[10.1016/j.jcp.2009.10.036](https://doi.org/10.1016/j.jcp.2009.10.036).
- Lauritzen, P. H., W. C. Skamarock, M. Prather, and M. Taylor, 2012: A standard test case suite for two-dimensional linear transport on the sphere. *Geosci. Model Dev.*, **5** (3), 887–901, doi:[10.5194/gmd-5-887-2012](https://doi.org/10.5194/gmd-5-887-2012).
- Leonard, B., A. Lock, and M. MacVean, 1996: Conservative explicit unrestricted-time-step multidimensional constancy-preserving advection schemes. *Mon. Wea. Rev.*, **124** (11), 2588–2606, doi:[10.1175/1520-0493\(1996\)124<2588:CEUTSM>2.0.CO;2](https://doi.org/10.1175/1520-0493(1996)124<2588:CEUTSM>2.0.CO;2).
- Leonard, B., M. MacVean, and A. Lock, 1993: Positivity-preserving numerical schemes for multidimensional advection. Tech. Rep. 106055, NASA.
- Leuenberger, D., M. Koller, O. Fuhrer, and C. Schär, 2010: A generalization of the SLEVE vertical coordinate. *Mon. Wea. Rev.*, **138** (9), 3683–3689, doi:[10.1175/2010MWR3307.1](https://doi.org/10.1175/2010MWR3307.1).
- Li, X., C. Chen, X. Shen, and F. Xiao, 2013: A multimoment constrained finite-volume model for nonhydrostatic atmospheric dynamics. *Mon. Wea. Rev.*, **141** (4), 1216–1240, doi:[10.1175/MWR-D-12-00144.1](https://doi.org/10.1175/MWR-D-12-00144.1).
- Lin, S.-J., and R. B. Rood, 1996: Multidimensional flux-form semi-Lagrangian transport schemes. *Mon. Wea. Rev.*, **124** (9), 2046–2070, doi:[10.1175/1520-0493\(1996\)124<2046:MFFSLT>2.0.CO;2](https://doi.org/10.1175/1520-0493(1996)124<2046:MFFSLT>2.0.CO;2).
- Mahrer, Y., 1984: An improved numerical approximation of the horizontal gradients in a terrain-following coordinate system. *Mon. Wea. Rev.*, **112** (5), 918–922, doi:[10.1175/1520-0493\(1984\)112<0918:AINAOT>2.0.CO;2](https://doi.org/10.1175/1520-0493(1984)112<0918:AINAOT>2.0.CO;2).

- Melvin, T., M. Dubal, N. Wood, A. Staniforth, and M. Zerroukat, 2010: An inherently mass-conserving iterative semi-implicit semi-Lagrangian discretization of the non-hydrostatic vertical-slice equations. *Quart. J. Roy. Meteor. Soc.*, **136** (648), 799–814, doi:[10.1002/qj.603](https://doi.org/10.1002/qj.603).
- Miura, H., 2007: An upwind-biased conservative advection scheme for spherical hexagonal-pentagonal grids. *Mon. Wea. Rev.*, **135** (12), 4038–4044, doi:[10.1175/2007MWR2101.1](https://doi.org/10.1175/2007MWR2101.1).
- Naughten, K. A., B. K. Galton-Fenzi, K. J. Meissner, M. H. England, G. B. Brassington, F. Colberg, T. Hattermann, and J. B. Debernard, 2017: Spurious sea ice formation caused by oscillatory ocean tracer advection schemes. *Ocean Model.*, **116**, 108–117, doi:[10.1016/j.ocemod.2017.06.010](https://doi.org/10.1016/j.ocemod.2017.06.010).
- Putman, W. M., and S.-J. Lin, 2007: Finite-volume transport on various cubed-sphere grids. *J. Comp. Phys.*, **227** (1), 55–78, doi:[10.1016/j.jcp.2007.07.022](https://doi.org/10.1016/j.jcp.2007.07.022).
- Schär, C., D. Leuenberger, O. Fuhrer, D. Lüthi, and C. Girard, 2002: A new terrain-following vertical coordinate formulation for atmospheric prediction models. *Mon. Wea. Rev.*, **130** (10), 2459–2480, doi:[10.1175/1520-0493\(2002\)130<2459:ANTFVC>2.0.CO;2](https://doi.org/10.1175/1520-0493(2002)130<2459:ANTFVC>2.0.CO;2).
- Shaw, J., and H. Weller, 2016: Comparison of terrain-following and cut-cell grids using a nonhydrostatic model. *Mon. Wea. Rev.*, **144** (6), 2085–2099, doi:[10.1175/MWR-D-15-0226.1](https://doi.org/10.1175/MWR-D-15-0226.1).
- Shaw, J., H. Weller, J. Methven, and T. Davies, 2017: Multidimensional method-of-lines transport for atmospheric flows over steep terrain using arbitrary meshes. *J. Comp. Phys.*, **344**, 86–107, doi:[10.1016/j.jcp.2017.04.061](https://doi.org/10.1016/j.jcp.2017.04.061).
- Skamarock, W. C., and A. Gassmann, 2011: Conservative transport schemes for spherical geodesic grids: High-order flux operators for ODE-based time integration. *Mon. Wea. Rev.*, **139** (9), 2962–2975, doi:[10.1175/MWR-D-10-05056.1](https://doi.org/10.1175/MWR-D-10-05056.1).
- Skamarock, W. C., and M. Menchaca, 2010: Conservative transport schemes for spherical geodesic grids: High-order reconstructions for forward-in-time schemes. *Mon. Wea. Rev.*, **138** (12), 4497–4508, doi:[10.1175/2010MWR3390.1](https://doi.org/10.1175/2010MWR3390.1).
- Smolarkiewicz, P. K., and J. Szmelter, 2005: MPDATA: An edge-based unstructured-grid formulation. *J. Comp. Phys.*, **206** (2), 624–649, doi:[10.1016/j.jcp.2004.12.021](https://doi.org/10.1016/j.jcp.2004.12.021).
- Smolarkiewicz, P. K., and J. Szmelter, 2011: A nonhydrostatic unstructured-mesh soundproof model for simulation of internal gravity waves. *Acta Geophys.*, **59** (6), 1109–1134, doi:[10.2478/s11600-011-0043-z](https://doi.org/10.2478/s11600-011-0043-z).
- Staniforth, A., and J. Thuburn, 2012: Horizontal grids for global weather and climate prediction models: a review. *Quart. J. Roy. Meteor. Soc.*, **138** (662), 1–26, doi:[10.1002/qj.958](https://doi.org/10.1002/qj.958).
- Steppeler, J., and J. Klemp, 2017: Advection on cut-cell grids for an idealized mountain of constant slope. *Mon. Wea. Rev.*, **145** (5), 1765–1777, doi:[10.1175/MWR-D-16-0308.1](https://doi.org/10.1175/MWR-D-16-0308.1).

- Steppeler, J., S.-H. Park, and A. Dobler, 2013: Forecasts covering one month using a cut-cell model. *Geosci. Model Dev.*, **6**, 875–882, doi:[10.5194/gmd-6-875-2013](https://doi.org/10.5194/gmd-6-875-2013).
- Thuburn, J., C. Cotter, and T. Dubos, 2014: A mimetic, semi-implicit, forward-in-time, finite volume shallow water model: comparison of hexagonal-icosahedral and cubed-sphere grids. *Geosci. Model Dev.*, **7** (3), 909–929, doi:[10.5194/gmd-7-909-2014](https://doi.org/10.5194/gmd-7-909-2014).
- Van Brummelen, G., 2013: *Heavenly mathematics: The forgotten art of spherical trigonometry*. Princeton University Press, 217 pp.
- Walko, R. L., and R. Avissar, 2008: The Ocean-Land-Atmosphere Model (OLAM). Part II: Formulation and tests of the nonhydrostatic dynamic core. *Mon. Wea. Rev.*, **136** (11), 4045–4062, doi:[10.1175/2008MWR2523.1](https://doi.org/10.1175/2008MWR2523.1).
- Weller, H., and A. Shahrokhi, 2014: Curl free pressure gradients over orography in a solution of the fully compressible Euler equations with implicit treatment of acoustic and gravity waves. *Mon. Wea. Rev.*, **142** (12), 4439–4457, doi:[10.1175/MWR-D-14-00054.1](https://doi.org/10.1175/MWR-D-14-00054.1).
- Weller, H., H. G. Weller, and A. Fournier, 2009: Voronoi, Delaunay, and block-structured mesh refinement for solution of the shallow-water equations on the sphere. *Mon. Wea. Rev.*, **137** (12), 4208–4224, doi:[10.1175/2009MWR2917.1](https://doi.org/10.1175/2009MWR2917.1).
- White, J., and J. J. Dongarra, 2011: High-performance high-resolution semi-Lagrangian tracer transport on a sphere. *J. Comp. Phys.*, **230** (17), 6778–6799, doi:[10.1016/j.jcp.2011.05.008](https://doi.org/10.1016/j.jcp.2011.05.008).
- White, L., R. Panchadharan, and D. Trenev, 2017: Flow simulation in heterogeneous porous media with the moving least-squares method. *SIAM J. Sci. Comput.*, **39** (2), B323–B351, doi:[10.1137/16M1070840](https://doi.org/10.1137/16M1070840).
- Xie, B., and F. Xiao, 2016: A multi-moment constrained finite volume method on arbitrary unstructured grids for incompressible flows. *J. Comp. Phys.*, **327**, 747–778.
- Zängl, G., 2012: Extending the numerical stability limit of terrain-following coordinate models over steep slopes. *Mon. Wea. Rev.*, **140**, 3722–3733, doi:[10.1175/MWR-D-12-00049.1](https://doi.org/10.1175/MWR-D-12-00049.1).
- Zerroukat, M., and T. Allen, 2012: A three-dimensional monotone and conservative semi-Lagrangian scheme (SLICE-3D) for transport problems. *Quart. J. Roy. Meteor. Soc.*, **138** (667), 1640–1651, doi:[10.1002/qj.1902](https://doi.org/10.1002/qj.1902).